THESIS

FLUME STUDY OF MECHANISMS RESPONSIBLE FOR PARTICLE SORTING IN GRAVEL-BED MEANDERING CHANNELS

Submitted by

Daniel White

Department of Civil and Environmental Engineering

In partial fulfillment of the requirements

For the Degree of Master of Science

Colorado State University

Fort Collins, Colorado

Fall 2019

Master's Committee:

Advisor: Peter Nelson

Ryan Morrison
Ellen Wohl

Copyright by Daniel White 2019

All Rights Reserved

ABSTRACT

FLUME STUDY OF MECHANISMS RESPONSIBLE FOR PARTICLE SORTING IN GRAVEL-BED MEANDERING CHANNELS

Meandering gravel-bed rivers tend to exhibit bed surface sorting patterns with coarse particles located in pools and fine particles on bar tops. The mechanism by which these patterns emerge has been explored in sand-bed reaches; however, for gravel-bed meandering channels it remains poorly understood. Here we present results from a flume experiment in which bed morphology, velocity, sediment sorting patterns, and bed load transport were intensively documented in a single-bend meandering channel. The experimental channel is 1.35 m wide, 15.2 m long, and its centerline follows a sine-generated curve with a crossing angle of 20 degrees. Water and sediment input were held constant throughout the experiment at 104.8 L/s and 230 kg/h, respectively, and measurements were collected under quasi-equilibrium conditions once the sediment input and output were approximately equal and the bed was essentially unchanging. Measurements of the three-dimensional velocity field indicate the development of a helical flow where near-bed velocity is directed toward the inner bank and flow at the surface is directed toward the outer bend. Calculated cross-stream bed load transport rates show that the trajectories of fine and coarse particles cross downstream of the bend apex, with fine sediment directed inward toward the point bar and coarse sediment directed toward the outer pool. Boundary shear stress, calculated from near-bed velocity measurements, indicates that in a channel with mild sinuosity, deposition of fine particles on bars is a result of divergent shear stress at the inside bend of the channel just downstream of the apex. The strong inward secondary currents that developed near the outside bend of the channel have little impact on the

fine sediment deposition occurring on the bar under the conditions of this study. Boundary shear stress at equilibrium in the upstream half of the pool was below the critical value for coarse particles (>8 mm), which were only found in the pool. Selective transport toward the sloped region connecting the pool and bar top was responsible for winnowing of fine particles in the pool. Similarly, boundary shear stress near the bar front at equilibrium was below the critical value for particles near the D_{50} of the bulk sediment feed (≤4 mm). Here, only fine particles were mobilized and transported downstream to the bar top. Fine and coarse sediment followed essentially identical trajectories through the meander bend, which contrasts earlier studies of sand-bedded meanders where fine and coarse particles cross paths. This suggests a different sorting mechanism for gravel bends. This experiment shows that a complex interaction of quasi-equilibrium bed topography, selective sediment transport, and currents that develop as a result of curved channel geometry are responsible for the sorting patterns seen in gravel bed, meandering channels.

ACKNOWLEDGEMENTS

I am grateful to my advisor Dr. Peter Nelson for his ongoing motivation to think about geomorphic processes from new perspectives and allowing me the opportunity to do so through research.

I'm grateful to my committee members Dr. Ryan Morrison and Dr. Ellen Wohl for their guidance and sharing their inspiring enthusiasm for river science.

Thank you to Ryan Brown and David Cortese for your assistance in the lab and for engaging in the activity of mentally processing the data we collected.

Finally, I thank my wife Rachelle for her unwavering encouragement to pursue my interests and the sacrifices she has made to help me reach my goals.

TABLE OF CONTENTS

LIST OF FIGURES

NOTATION

D	grain size.
D_{50}, D_{84}	grain size for which 50 and 84% of particles is finer
g	acceleration due to gravity
h	flow depth
m	meander wavelength
n	normal distance from channel centerline
N	channel geometric coefficient calculated from n/R
p	sediment porosity
q_n	cross-stream unit sediment transport rate
q_s	downstream unit sediment transport rate
R	local radius of curvature
s	streamwise distance downstream
t	time
u_*	shear velocity
$u(z)$	velocity at height, z, above the bed

u_s local average streamwise measured velocity

u_n local average transverse measured velocity

z_0 roughness height

ϕ angle of channel centerline with respect to horizontal

ω channel angle of departure

τ Shear stress

τ^* dimensionless shields stress

τ_{rg}^* reference shields stress for gravel, 0.0386

ρ density of water

η Bed elevation

κ von Karman's constant, 0.4

1. Introduction

Spatial variation in bed-surface sediment particle size is a common characteristic of sand- and gravel-bedded alluvial rivers (Bridge, 1977; Buffington & Montgomery, 1999; Clayton, 2010; Clayton & Pitlick, 2008; Dietrich & Smith, 1984; Dietrich & Whiting, 1989; Jackson, 1975; Julien & Anthony, 2002; Lisle & Madej, 1992; Nelson et al., 2010; Paola & Seal, 1995; Gary Parker & Andrews, 1985; Powell, 1998). Bed-surface sediment affects near-bed velocity and flow roughness (van Rijn, 2007), local sediment transport rates, and particle mobility (e.g., Parker, 1990; Venditti et al., 2010; Wilcock & Crowe, 2003) and the health of riverine ecosystems (Chapman, 1988; Kondolf & Wolman, 1993; Wood & Armitage, 1997).

Meandering channels typically develop fine point bars on the inside of bends, and coarse pools on the outside of bends (Bridge, 1977; Clayton, 2010; Dietrich & Whiting, 1989). Straight channels, however, develop alternating bars which exhibit coarse sediment patches located on bar tops with fine particles in the pools (Keller & Florsheim, 1993; Lanzoni, 2000; Nelson et al., 2010; Thompson et al., 1999).

Bed-surface sorting is the result of complex interactions between the channel planform, bed topography, the size distribution and volume of sediment supply, bed roughness due to local particle size, flow stage, and discharge. Locally nonuniform flow due to variations in planform and bed morphology produces spatial variations in shear stress that may be accommodated by deposition of fine material and formation of armored patches (Dietrich & Whiting, 1989; Paola & Seal, 1995; Parker & Andrews, 1985). Bed topography also gives rise to gravitational forces facilitating cross-channel movement of particles into pools. In curved channels, counteracting forces due to secondary circular currents may overcome those gravitational forces and selectively transport finer gravel particles toward the bar (Parker & Andrews, 1985).

The pattern of coarse bars and fine pools in straight gravel-bed channels was investigated experimentally by Nelson et al. (2010). They observed "forced" bar topography directing flow from the bar to the pool, resulting in diverging boundary shear stress over the bar top and converging shear stress in the pool. The declining magnitude of boundary shear stress over the bar produced increasingly size-selective sediment transport, so that fine particles were preferentially transported away from the bar top and into the pool, resulting in a coarse bar and fine pool. These forced bars were spatially and temporally persistent and exerted a strong control on flow directions.

Detailed observations of flow and sediment transport in meandering channels have largely been constrained to sand-bedded rivers, where shear stresses are high enough that size-selective or partial sediment transport generally does not occur. In a series of studies using data from Muddy Creek, a sinuous sand-bedded alluvial stream, Dietrich (1987), Dietrich & Smith (1984), and Dietrich & Whiting (1989) performed extensive analyses of physical processes that influence the development of sorting patterns. Detailed bed load transport measurements showed that the locus of fine and coarse sediment particles cross paths downstream of the apex of the bend as a result of inward directed shear stress moving fine particles toward the bar while coarse particles tended to move toward the pool. Convective accelerations at the outside bend of the channel resulted in spatially varied shear stresses that influence the trajectory of particles and contributed to the development of fine bars and coarse pools.

Additionally, theoretical models of sorting in bends point to the potential balance of forces due to gravity and secondary helical flow structures to develop sorting patterns. Parker & Andrews (1985) developed a theoretical model of sorting in bends that describes the forces acting on grains of varied particle sizes on the transverse slope of a bar. They state that the ratio

of gravitational forces pulling sediment down to the pool to the force responsible for down and cross stream drag is greater for larger sediment particles, resulting in fine bars and coarse pools. They also developed a theoretical explanation describing the sediment transport trajectory of the coarsest sediment particles through meandering channels. Similarly, Ikeda (1989) showed that particles of greater mass more strongly feel the forces of gravity resulting in coarse pools. He also asserted that in a theoretical channel of constant curvature, sediment particles would follow a trajectory parallel to the channel centerline balanced by the transverse gravitational and opposing drag forces caused by secondary currents.

We generally lack detailed observations of flow, topography, sediment transport, and sorting in gravel bed meandering rivers, so it is not clear to what extent size-selective or partial sediment transport is responsible for sorting and topography in these channels, or how this interacts with the three-dimensional flow field that develops in curved channels. Dietrich et al.'s (1984, 1987, 1989) observations of sediment transport and sorting in a sand-bed meander indicated that fine and coarse particles follow different trajectories through the bend, leading to the development of a fine bar and coarse pool. Here, we investigate whether the same mechanism occurs in a gravel-bed meander bend, and we hypothesize that size-selective transport may be an important control on the development of fine bars and coarse pools. In this paper we present detailed measurements of topography, bed sorting patterns, the flow field, and the sediment transport field in an experimental meander bend so that we may improve our understanding of the morphodynamics of gravel-bed meandering rivers. We also explore, through detailed observation, how curvature-induced secondary flows influence sorting in a gravel-bed meander.

2. Methods

2.1 Experimental setup

We conducted a flume experiment at Colorado State University's Hydraulics Laboratory in a channel with a single meander bend. The overall goal of the experiment was to develop steady-state flow, bed topography, and sorting, and then thoroughly document the flow field, sediment transport field, bed topography, and sorting patterns so that mechanisms responsible for the development of bars, pools, and sorting patterns could be discerned.

The flume centerline was defined by a sine-generated trace as described by Langbein & Leopold (1966):

$$\phi = \omega \sin\left(2\pi \frac{s}{m}\right) \tag{1}$$

where ϕ is the angle of the channel centerline with respect to horizontal, ω is the angle of departure (20 degrees in the experimental setup), s is the distance downstream along the channel centerline, and m is the meander wavelength (12.58 m in our experiment). The flume had a constant width of 1.35 m, and 1.5-m-long straight entrance and exit reaches resulting in an overall centerline of 15.58 m length (see Figure 1). The flume was initially filled with a sediment mixture to a depth of 30 cm and screeded flat to a slope of 0.007. See Appendix A for photos of the experiment setup.

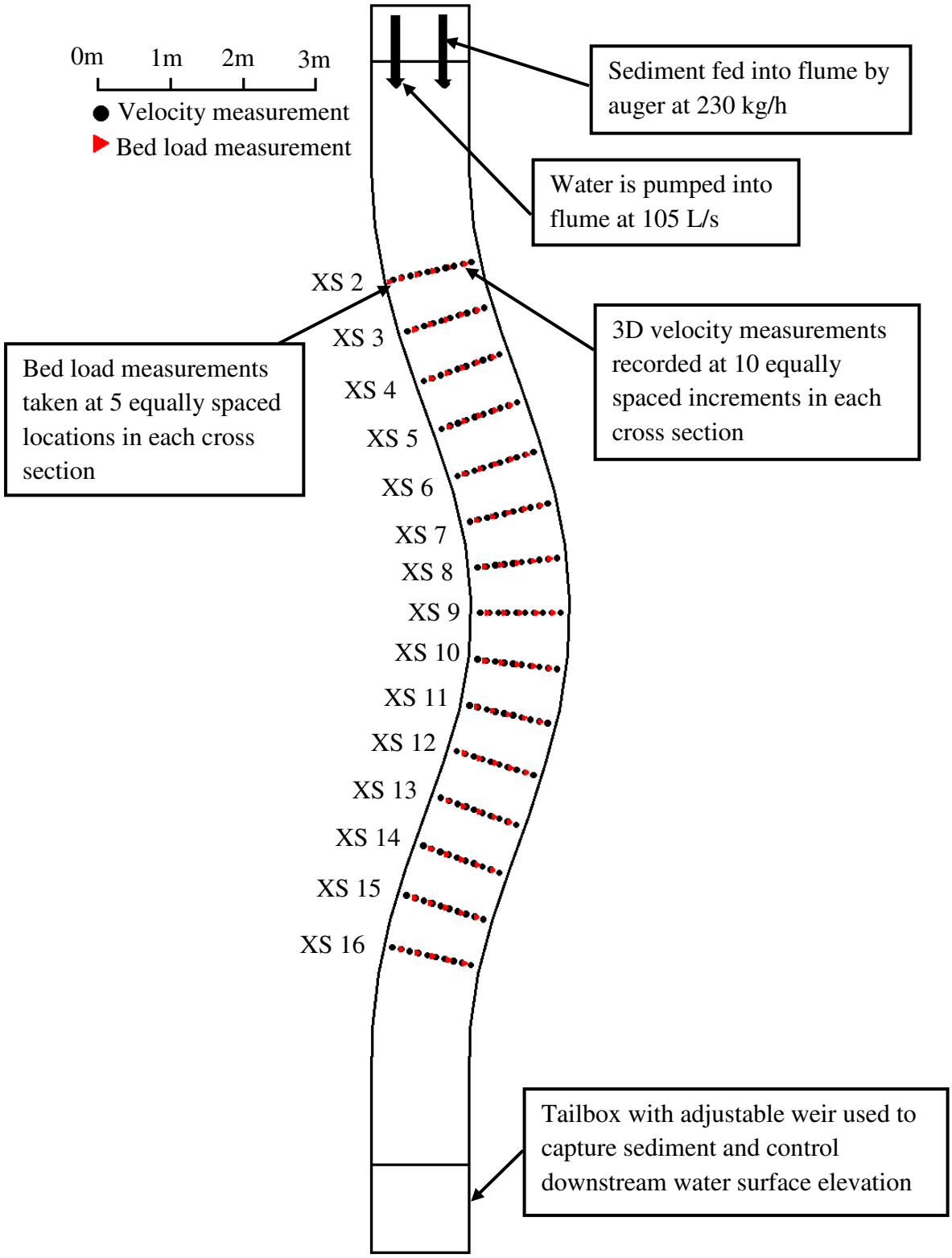

Figure 1. Flume setup schematic

A 40-hp pump maintained a constant water discharge of 105 L/s to the flume. The water surface elevation at the downstream end of the flume was controlled by an adjustable tailgate to maintain uniform conditions in the exit reach of the flume. Sediment was fed into the upstream end of the flume with a variable-speed auger. The sediment feed rate was held constant at 230 kg/h for the duration of the experiment.

The channel geometry, flow, and sediment feed rate were selected to achieve an average dimensionless shear stress ($\tau^* = \frac{\tau}{((\rho_s - \rho)gD_{50})}$, where τ is the boundary shear stress, ρ_s and ρ are the densities of sediment and water, g is gravitational acceleration, and D_{50} is the median bed sediment size) approximately twice the critical value (assumed to be $\tau_c^* = 0.0386$) to produce bar-pool morphology and transport sediment primarily as bed load. The sediment feed was composed of a mixture ranging in size from fine sand to pebbles roughly from 0.2 mm to 8.0 mm, with a median grain size (D_{50}) of 3.3 mm (Figure 2). This range of sediment sizes was selected to ensure measureable sorting patches. Sediment exiting the downstream end of the flume was trapped in a tailbox. This sediment was dried and weighed between flume operation periods to determine the total bed load flux exiting the channel.

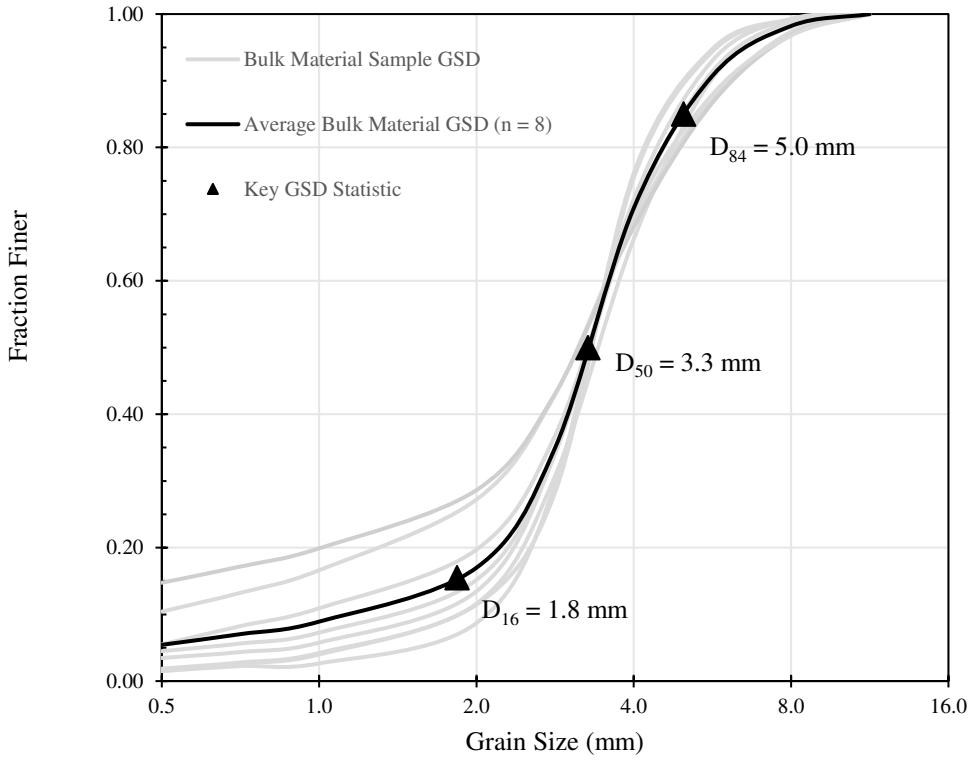

Figure 2 Grain size distribution of bulk material sediment feed. Before each flume run period, a sample was taken from the bulk material and sieved. The grey lines in the figure represent these sieved grain size distributions. The black line represents the average of each bulk sample distribution.

We would run the flume until the tailbox filled with sediment, typically for periods ranging from 90 to 240 minutes, at which point the flow and sediment feed would be shut down, the flume drained, and bed measurements collected as described below. We did not visually observe any significant bed changes resulting from stopping or starting the flume over the course of the experiment. The initial experimental phase of establishing quasi-equilibrium conditions, defined as conditions where the total sediment discharge was roughly equal to the sediment feed rate, lasted approximately 15 hours. Once quasi-equilibrium was achieved, the experiment continued

for another ~40 hours of run time, during which detailed flow and sediment transport measurements were made as described below.

2.2 Bed load measurements

To characterize flow and bed load transport throughout the meander bend, we established 15 cross sections along the bend oriented orthogonal to the channel centerline, with an average spacing along the centerline of 0.7 m. Five bed load samples were collected at evenly spaced increments in each cross section using a Helley-Smith sampler with a 7.6 cm x 7.6 cm opening and fine mesh nylon bag (see Appendix A for photos of bed load sampling procedure.) The sampler was oriented orthogonal to the cross-section, so the samples represent the downstream component of the local bed load transport vector. Sample times varied from 30 to 120 seconds depending on the local rate of sediment transport. Areas where little sediment transport was observed, such as bar tops, required longer sampling times to capture enough sediment particles for analysis. A large sediment sample time is desirable when analyzing transport by size fraction. We found, however, that holding the sampler on the bed longer than 120 seconds in areas where sediment transport was low resulted in small scour features around the sampler. To minimize impact to bed topography while maximizing sample size, we found it necessary to stop bed load measurements when slight sampling-induced topographic alterations appeared. Because of this, smaller sample times are a likely factor in the variation of total measured sediment transport between cross sections. Each sediment sample was then dried, sieved and used to assess the sediment transport by size fraction throughout the channel. Total downstream sediment transport at each section was calculated by integrating the bed load samples over the width of the channel.

2.2.1 Calculation of cross-stream bed load transport rates

As in prior studies where downstream sediment transport rates have been measured under quasi-equilibrium conditions, (Dietrich & Smith, 1984; Nelson et al., 2010) we used sediment continuity and an assumption of steady-state to calculate cross-stream bed load transport rates. We first normalized the magnitude of the downstream bed load samples so that the integrated transport at each cross section was the mean value. The coefficient of variation for the total bed load transport measurements was 0.3, which is similar to values reported in other studies (0.25 at Muddy Creek (Dietrich and Smith, 1984), and 0.2 at St. Anthony Falls Laboratory (Nelson et al., 2010)). These normalized downstream transport rates were then used to compute cross-stream rates as described below.

Following Smith and McLean (1984) the sediment continuity equation in an orthogonal curvilinear coordinate system can be written:

$$\frac{1}{1-N}\frac{\partial q_s}{\partial s} - \frac{q_n}{(1-N)R} + \frac{\partial q_n}{\partial n} = -(1-p)\frac{\partial \eta}{\partial t} \tag{2}$$

where q_s is the streamwise unit sediment discharge, q_n is the cross-stream unit sediment discharge, N is a metrical coefficient defined as n/R, n is the normal distance from the channel centerline (positive to the left bank), R is the local radius of curvature of the channel centerline, s is the streamwise distance downstream, p is the sediment porosity, η is the bed elevation, and t is time. Under quasi-equilibrium conditions, the bed height, η, remains constant and therefore the right side of the equation becomes zero. Equation 2 can then be solved by establishing a boundary condition of $q_n = 0$ at the right bank, (at $n = -w/2$, where w is the channel width). This yields an expression for q_n:

$$q_n = -\frac{1}{1-N}\int_{-\frac{w}{2}}^{n}\frac{\partial q_s}{\partial s}\partial n \quad (3)$$

This relation can be applied for each size class in the grain-size distribution to compute size-specific cross-stream bed load transport rates. We discretized this function to calculate q_n for all size classes at each bed load sampling location from the second cross section downstream. The derivatives of q_s were approximated as forward differences, so that the first calculated values of q_n were in the second cross section where sediment transport measurements were taken.

2.3 Topography measurements

Bed topography was measured throughout the experiment using structure-from-motion (SfM) photogrammetry. During periods when the flow was shut down and the bed load trap was emptied, we photographed the bed with an 18-megapixel Cannon Rebel T3i digital SLR camera with an 18-55 mm lens (typically set to a focal length of 25 mm) mounted to a tripod system that was connected to a rolling cart that moved up and down the length of the flume. The camera was oriented approximately 1.5 meters above and orthogonal to the bed. Photos were taken at approximately 0.2 m increments across the channel and in the downstream direction. The photos were taken with roughly 70% overlap to increase the accuracy of the image processing. Between flume run times, up until equilibrium bed conditions were reached, approximately 250 photos were taken and used to develop three-dimensional topographic point clouds using Agisoft Metashape, and once equilibrium bed conditions were reached, 550 photos were used to develop a higher-resolution point cloud with less than 0.5 mm point spacing. Photos were taken in JPEG file format for compatibility with MetaShape. The following workflow was followed to generate a dense point cloud in Metashape: 1) Import images to the software and align with 'high' accuracy; 2) Identify ground targets at locations surveyed prior to the flume run; 3) Optimize

images and camera locations; 4) Generate dense point cloud with 'high' quality. The dense point cloud generated in Metashape was opened in CloudCompare where equilibrium bed conditions were evaluated by comparing sequential point clouds. Bed elevation changes beyond t = 15 hours were negligible. In CloudCompare, a polyline of the flume planform geometry was used to clip the unnecessary point data, and the data were then resampled to 5 mm spacing to reduce processing times.

After bed load and flow velocity measurements were taken and prior to the collection of photos for the high-resolution SfM point cloud, the sediment feed and flow were shut off while simultaneously raising a downstream weir on the tailbox. The increased downstream water surface elevation and halted flow resulted in negligible flow velocities in the channel as the flume drained slowly, preserving the topography of the bed.

The SfM point clouds were interpolated onto a rectilinear grid with spacing of 0.01 m using a kriging algorithm in Golden Software's Surfer program. Cells that fell outside the flume boundaries were assigned NODATA values. For the purpose of comparing bed surface elevation after each flume run, the average value at each longitudinal gridded increment (y values, ignoring NODATA containing cells) was calculated and plotted as a function of horizontal distance downstream (the incremental grid number (x index) multiplied by 0.01 m). A detrended topographic bed elevation map was generated by calculating the mean downstream Cartesian slope over the channel length and offsetting the gridded increments in each column (y values) such that the mean elevation at each column was equal.

2.4 Sorting measurement

Sediment sorting patterns were mapped by visual observation following the method described by Nelson et al. (2009) and Nelson et al. (2010). The bed was divided into 5 facies, or

patch types based on a visual assessment of the local average grain size and degree of sorting. Grain-size distributions for each patch type were measured noninvasively using digital photographs. Photos were taken orthogonal to the surface of the bed in each patch type, capturing an area approximately 25 by 40 cm. Each photo was opened in MATLAB and divided into an equally spaced grid of 100 points. The intermediate axis of the particle at each grid intersection point was measured by drawing a line across the particle (see Appendix D for an example of this method). A steel ball bearing 3.175 mm in diameter was placed in each of the photos as a reference to determine scale of each photograph; this scale was used to convert the measured sediment diameters from pixels to millimeters.

2.5 Velocity measurement

Velocity, water surface elevation, and bed elevation measurements were taken approximately simultaneously at 10 equally spaced points in each of the 15 cross sections as seen in Figure 1. Water surface elevations were measured with a point gauge and referenced to the local coordinate system. A side-looking Nortek Vectrino+ acoustic Doppler velocimeter (ADV) was used to measure three-dimensional flow velocities near the water surface and in shallow areas such as over the bar top. Appendix A shows photographs of the experimental setup for collecting velocity measurements. ADV measurements were collected at a frequency of 100 Hz over 30 seconds. In areas of flow deeper than 8 cm, velocity profiles were collected using a downward-looking Nortek Vectrino Profiler, a profiling acoustic Doppler velocimeter (P-ADV). The P-ADV measures three-dimensional velocity at 100 Hz in thirty 1-mm-high bins spanning a 3 cm vertical window. In areas where flow depth exceeded 10 cm, multiple, stacked, 3-cm velocity profiles were captured with the P-ADV, measuring as much of the water column as possible. Bed elevations were measured using a point gauge immediately prior to the velocity measurements.

The P-ADV is also capable of measuring the depth from the sensor to the bed. In our analysis, the P-ADV-measured bed elevation was used and verified with the point gauge reading.

The velocity measurements were plotted in MATLAB with isoline-generated contour plots overlain by vectors representing the cross stream and vertical velocity components. This was done for all cross sections where velocity measurements were taken.

2.6 Shear stress calculations

We used the velocity profiles to calculate boundary shear stress throughout the channel by fitting a logarithmic function to the near-bed portion of the velocity profile (Wilcock, 1996). A logarithmic velocity profile is expressed mathematically through the law of the wall:

$$u(z) = \frac{u_*}{\kappa} \ln\left(\frac{z}{z_0}\right) \tag{4}$$

where $u(z)$ is the velocity at the height above the bed z, u_* is the shear velocity, defined a $u_* \equiv \sqrt{\tau/\rho}$, where τ is the boundary shear stress and ρ is the water density, z_0 is the roughness height above the bed where $u(z) = 0$, and $\kappa = 0.4$ is von Karman's constant.

The velocity $u(z)$ is the resultant of measured downstream and cross-stream components of the velocity

$$u(z) = \sqrt{|u_s(z)^2| + |u_n(z)^2|} \tag{5}$$

where u_s is the local average streamwise measured velocity and u_n is the local average measured transverse velocity. The measured velocity profiles were assessed using the suggested guidelines as stated in (Wilcock, 1996) that logarithmic profiles should be present where $3D_{84} < z < h/5$ and $h/D_{84} > 15$. For each of the 150 measured velocity profiles, we plotted $u(z)$ vs $\ln(z)$ and

identified regions that met the criteria and followed a clear linear trend (see Figure 3). Equation 4 can be rewritten as

$$\ln(z) = \frac{\kappa}{u_*} u(z) + \ln(z_0) \tag{6}$$

so that the slope of a linear regression of $\ln(z)$ vs. $u(z)$ corresponds to k/u_*, yielding an estimate of the shear velocity and therefore the boundary shear stress.

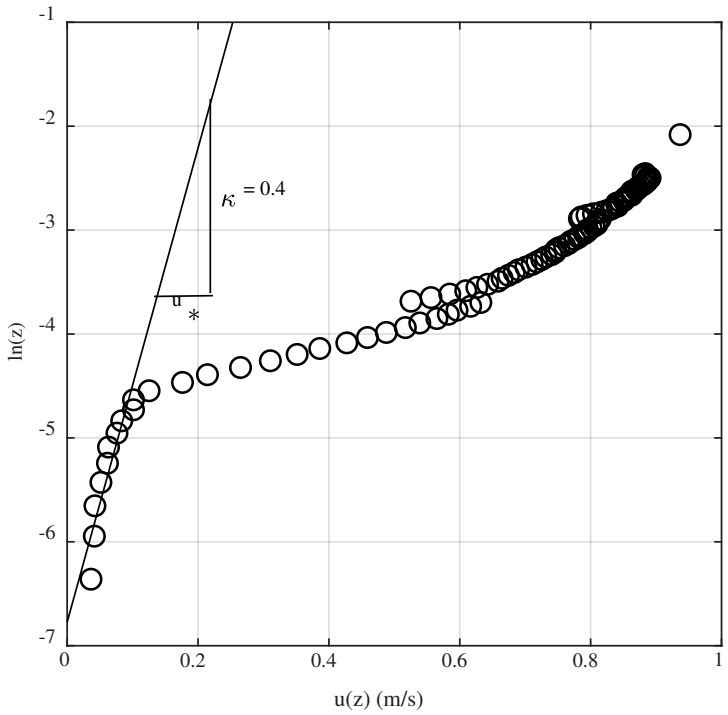

Figure 3. Stacked measured velocity profile showing the logarithmic relation of flow depth to velocity near the bed in a patch of fine sediment particles. At a height above the bed of approximately 0.012 m ($ln(z)$ = -4.4), the profile diverges from the logarithmic relationship, so only the near-bed values are used to compute shear stress. The line shows the linear fit to the near-bed profile.

In some locations the flow depth was too shallow to measure full velocity profiles. In these areas, we measured near-surface and near-bed velocities with the side-looking Vectrino ADV. As described by Dietrich & Whiting (1989) and Nelson et al. (2010), we estimated shear stress at

these locations with a single velocity measurement. Here, equation (6) was still used, and we used the local bed surface grain-size distribution to estimate the roughness height $z_0 = 0.1D_{84}$ (Dietrich & Whiting, 1989; Leopold & Wolman, 1957).

3. Results

3.1 Equilibrium topography

Sediment transport exiting the flume was initially much higher than the feed rate, exceeding 600 kg/h (Figure 4a). The high initial sediment transport rate reflects about 6 cm of scour that occurred at the downstream end of the flume (Figure 4b) and subsequent erosion of the upstream half of the flume bed as the slope relaxed from its initial value of 0.007 to a quasi-equilibrium value of 0.005. After 15 hours of run time, sediment transport at the flume outlet was approximately equal to the sediment feed rate (Figure 4a) and the bed profile became generally unchanging (Figure 4b).

Equilibrium bed topography was characterized by point bars that developed on the left side of the channel upstream of the bend apex and on the right side of the channel downstream of the bend apex, and adjacent pools along the opposite sides of the channel (Figure 5). Due to the restricted length of the basin in which the flume was constructed, conditions at the upstream end of the bend did not become fully developed. The relief between the bar and pool upstream of the bend apex was approximately 15 cm, and the relief downstream of the apex was about 25 cm. Because of likely entrance effects, we focus our analysis of bed topography and sorting on the region downstream of the bend apex (x = 7 m in Figure 5).

(a)

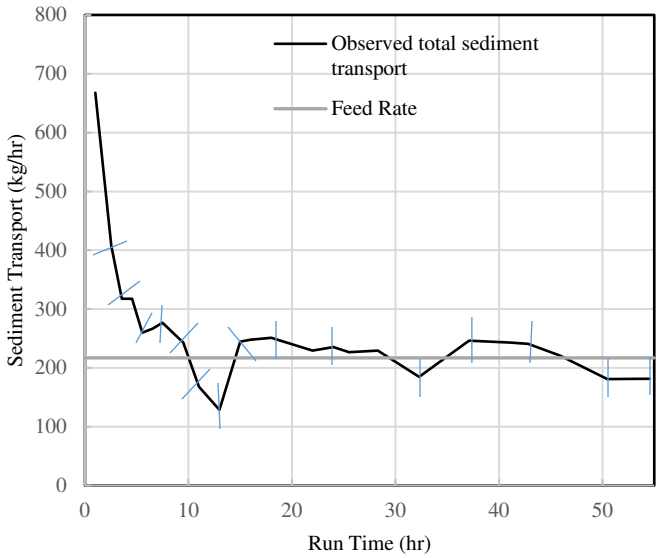

(b)

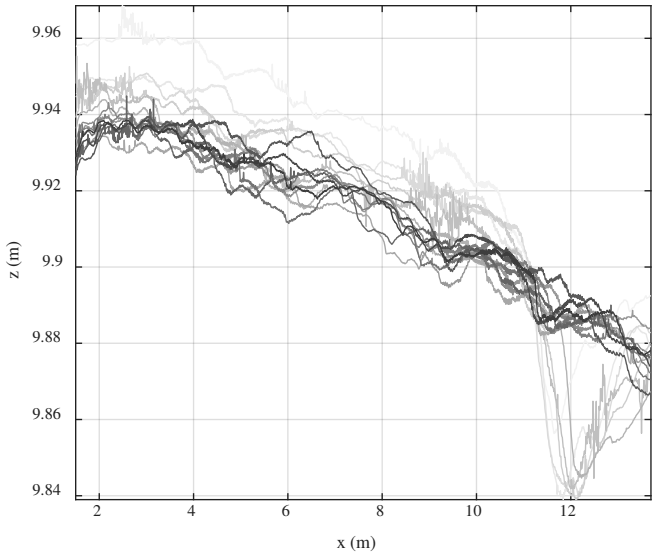

Figure 4. (a) Measured sediment transport rate as defined by dry weight of sediment in the tail box over flume run time contributing to the tailbox sample. The tick marks intersect the curve where bed topography was measured. (b) Bed elevation and evolution of a quasi-equilibrium conditions. The lines grow increasingly dark with flume run time at each bed topography measurement and correspond to the flume run time of tick marks in Figure 4a. Notice that the darkest lines converge to a state of roughly equal slope throughout the channel, and tend to change very little with time.

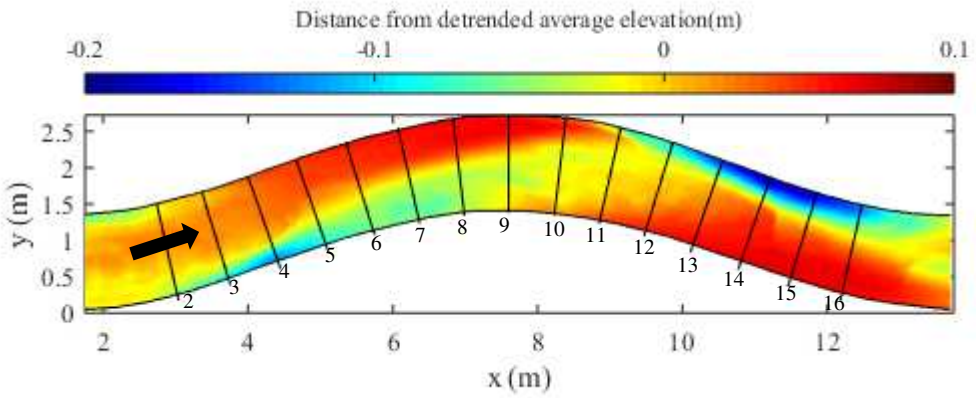

Figure 5. Detrended equilibrium bed topography. Cool shaded areas are topographically low (pools) and warm shaded areas are topographically high (point bar).

3.2 Sorting

The sorting pattern observed under quasi-equilibrium conditions is shown in Figure 6a. The bed was categorized into five patch types, and the grain-size distributions of these patch types are presented in Figure 6b. Upstream of the bend apex, longitudinal patches of medium-fine sediment developed, which probably resulted from flow over cinderblocks placed at the upstream entrance to the flume to dissipate energy and prevent upstream scour. There were one- to two-inch spaces between the blocks where flow passed through and affected the topography and sorting patterns until just upstream of the bend apex. Where flows were deflected as the curvature of the planform increased, there was a patch of coarse particles (D_{50} = 3.7 mm) that is consistent with observations made at the other pool in the channel and in other studies.

The point bar downstream of the bend apex exhibited a downstream fining pattern, with medium (D_{50} = 2.6 mm) sediment at the apex of the bend transitioning to fine (D_{50} = 1.3 mm) roughly one meter downstream, which in turn transitioned to medium fine particles (D_{50} = 1.6 mm) further downstream.

At the outside bend, a coarse sediment patch located in the pool extended approximately 2 meters along the channel edge. The bed then becomes increasingly finer, transitioning to a medium-coarse patch, and further downstream to medium. A small medium-fine patch is located adjacent to the coarse pool, which may be the result of selective transport as secondary currents are strongly developed at this location.

At the apex, in the center of the channel, a ribbon of medium-fine bed material extends downstream, eventually transitioning to medium. Topographically, this is located at the front of the bar. A unique bimodal distribution was found in the medium-coarse patch located downstream of the pool at the outside bend. However, the D_{50} here did fall between those of the coarse and medium facies types.

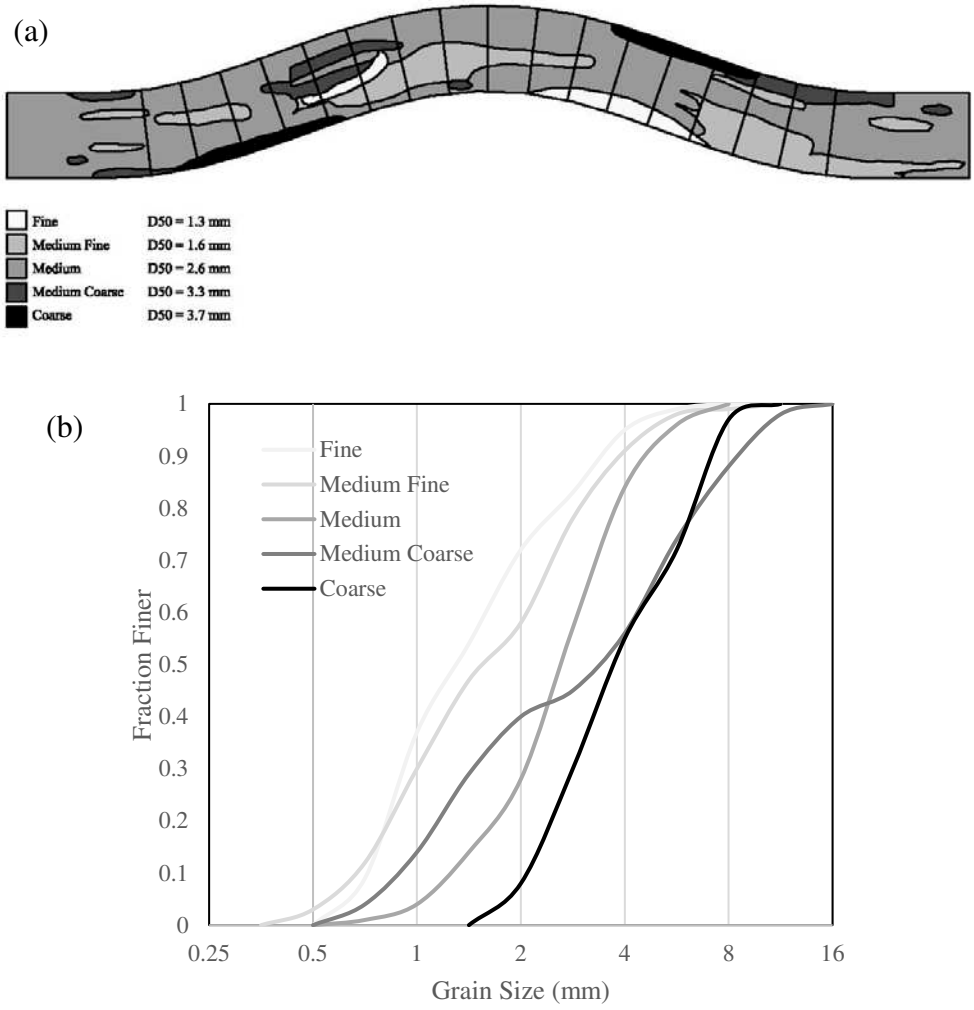

Figure 6. (a) Sediment sorting pattern observed at equilibrium bed topography. A fine patch developed downstream of the bend apex on the inside of the curve. A clear coarse patch developed at the outside of curve in the pool. (b) Grain-size distributions for each facies type. The bimodal medium-coarse patch was located just downstream of the pool.

3.3 Bed load transport

Bed load transport measurements collected under quasi-equilibrium conditions are depicted in Figure 7. The locus of maximum transport shifts from the inside to the outside edge of the channel a short distance downstream of the bend apex. In observing patterns of sorted patches, it is useful to identify locations where total normalized bed load transport changes dramatically in similar cross section stations. Perhaps the most drastic example of this behavior is seen in Figure

7 at cross sections 10 and 11, where the total bed load transport near the inside edge of the channel drops from 0.16 kg/m/s to 0.014 kg/m/s. It is at this same location that the bed sorting pattern shifts from medium (D_{50} = 2.6 mm), to fine (D_{50} = 1.3mm). The sediment transport near the outside bend at cross sections 11 and 12 shows a sharp increase, rising from 0.05 kg/m/s to 0.17 kg/m/s in this location, the sorting pattern shifts from medium (D_{50} = 2.6 mm) to coarse (D_{50} = 3.7 mm).

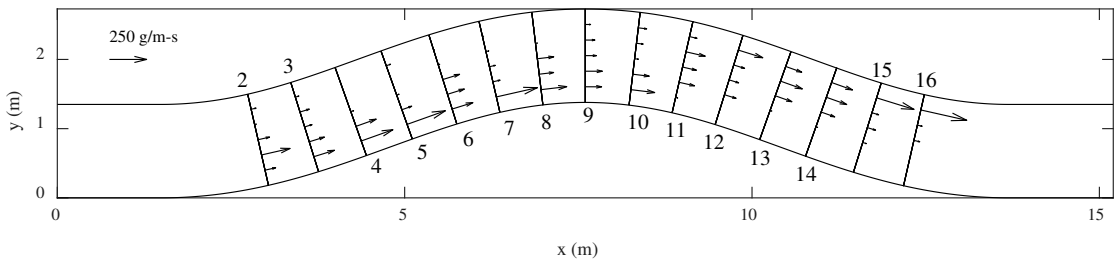

Figure 7. Magnitude of unit bed load samples measured through the flume. The region of high bed load transport shifts from one side of the channel to the other downstream of the bend apex.

Figure 8 depicts vectors of sediment transport for the coarse sediment (larger than 4 mm, Figure 8a) and fine sediment (finer than 2 mm, Figure 8b), where the cross-stream components of the transport vectors were computed using the continuity equation as described in Section 2.2.1. In general, the coarse sediment moves from the inside to the outside of the channel at the bend apex and just downstream (cross-sections 9 - 11). At cross-sections 11 and 12 on the outside bend of the channel, the direction of the vector for coarse particles shifts from pointing toward the pool on the outside channel bend, to a trajectory pointing out of the pool and onto the sloped section of bar.

The trajectories of fine sediment (Figure 8b) were similar to those of coarse particles; however, at the top of the point bar (cross-section 10), fine sediment transport was oriented

toward inner bank at both sampling locations closest to the right bank, while coarse sediment at the same location was directed toward the outer bank and pool (Figure 8a).

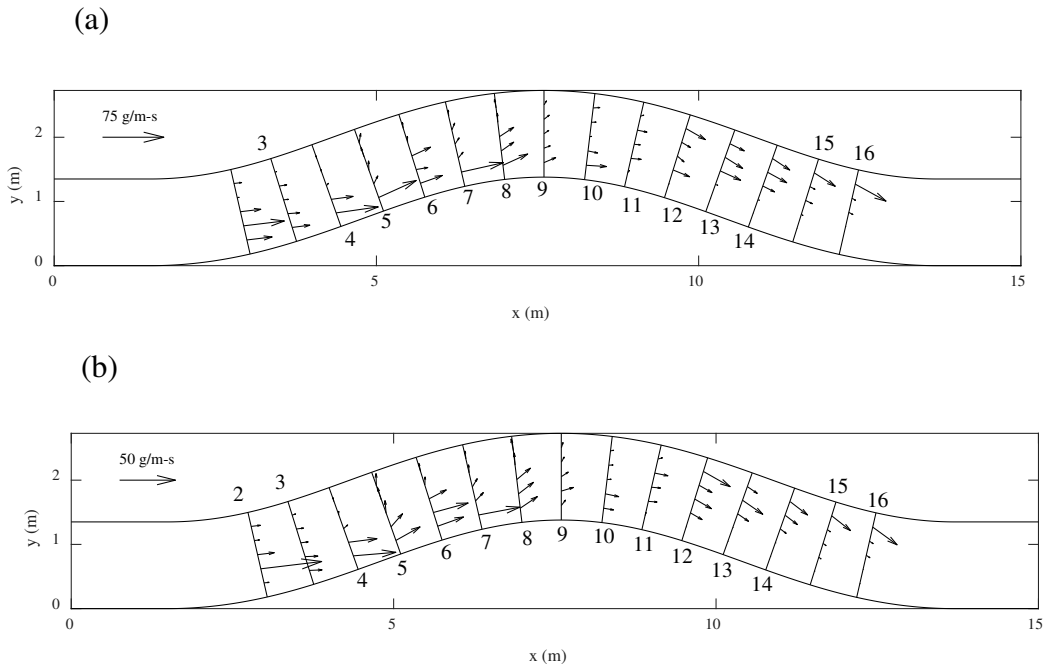

Figure 8. (a) Trajectories of sediment particles coarser than 4 mm. (b) Trajectories of sediment particles finer than 2 mm. At the cross section downstream of the bend apex, the overall pattern of coarse particles is to shift toward the outside of the channel. The fine sediment particles here have a slight inward overall transport direction. The coarse and fine particles follow very similar pattern of transport away from the pool at cross sections 12 through 15.

3.4 Velocity flow field and secondary currents

Figure 9 shows the measured three-dimensional velocity field at cross sections from the bend apex (cross section 10) to the downstream pool (cross section 14). At the bend apex (cross section 10), the high-velocity core was on the left side of the channel, with flow laterally oriented toward the right bank almost everywhere. There are indications, however, of small secondary currents on the inside bend, likely caused by the turbulent fluctuations in flow that develop in the shadow of the channel curve.

Moving downstream, the high-velocity core shifts to the left side of the channel over the developing pool (cross sections 13 and 14), and a well-developed secondary circulation with near-bed flow directed toward the inner bank of the bend. The secondary circulation is confined to a fairly small portion of the total channel width until 3 meters downstream of the bend apex (cross section 14). Not until cross-section 15 do the secondary circular currents send near-bed flows past the channel centerline and onto the bar on the right side of the channel. See Appendix C for plots of velocity profiles measured through the entire channel.

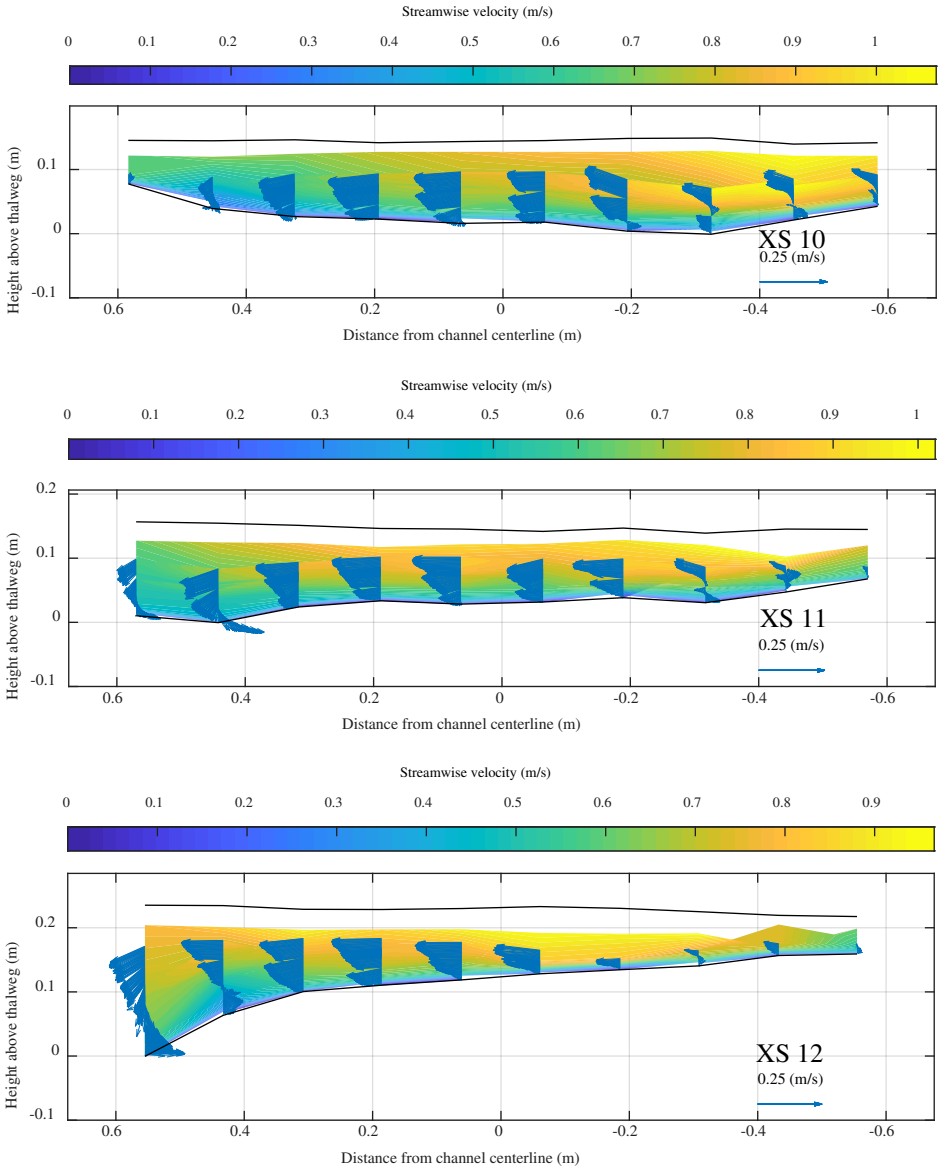

Figure 9. Cross sectional plots of 3D velocity measurements taken at cross sections 10, 11, 12, 13 and 14. The dark blue to yellow contours represent the magnitude of the streamwise velocity. The blue arrow vectors represent the transverse and vertical components of the velocity measurements taken at 1 mm increments through the water column. There is a lack of data near the water surface, because the Vectrino Profiler P-ADV required full submergence to function properly. The near-surface velocity values were supplemented with measurements taken by a single point velocimeter that required less submergence.

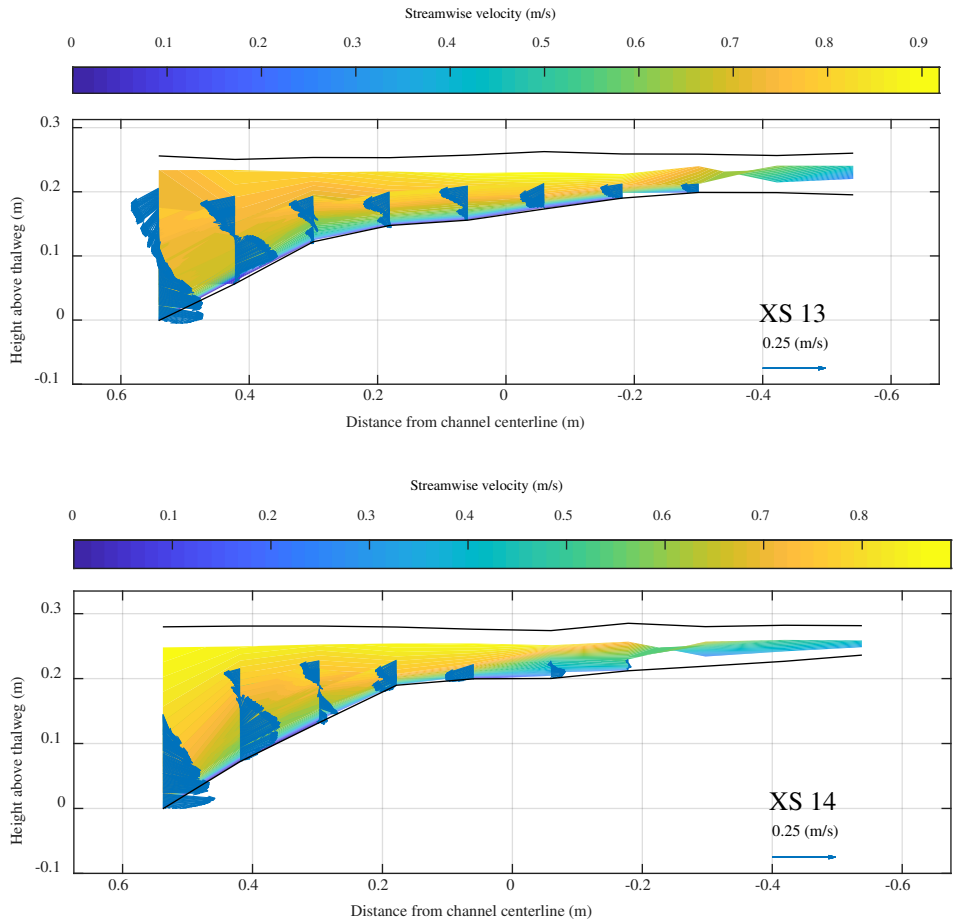

Figure 9 (continued) See caption on previous page.

3.5 Shear stress field

Figure 10a shows the boundary shear stress field computed from the velocity measurements, and Figure 10b presents the data as a contour map generated using the MATLAB contour function, which projects interpolated values between measurement points on a grid. The general shear stress pattern is corroborated by calculations from a 3D hydrodynamic model (Appendix B). The stress vectors share the same direction as near-bed velocity. The region of maximum shear stress shifts from the inside to outside of the bend past its apex. From cross-section 9 to 10, stress drops to almost zero at the same location where the finest sorting patch begins (Figure 5a).

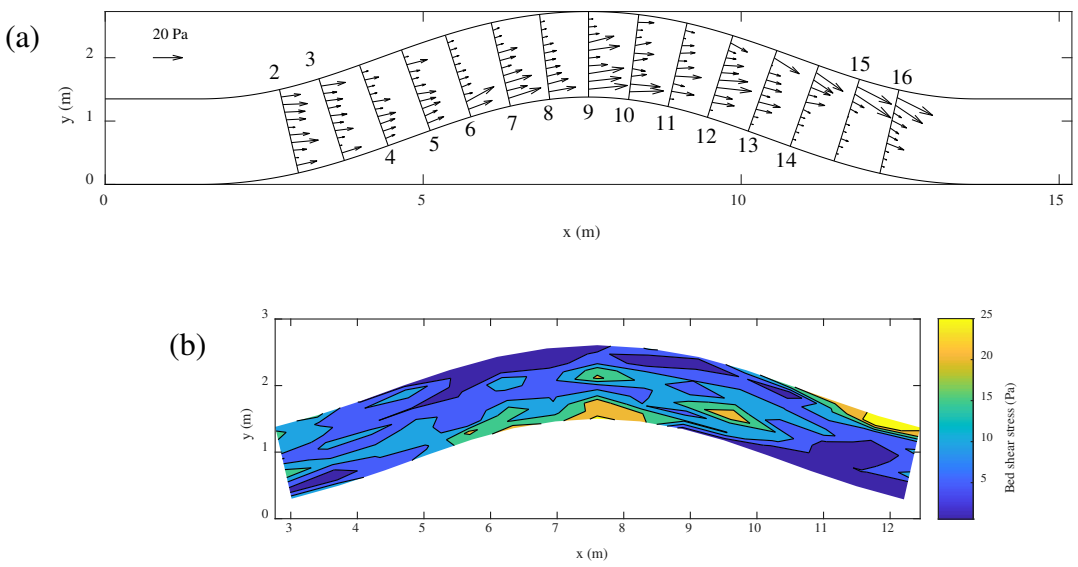

Figure 10. (a) Boundary shear stress calculated from near-bed velocities. The region of high shear stress shifts from inside to outside past the bend apex. The shear stress in the upper half of the pool is low although a patch of coarse sediment was found here. Shear stress vectors converge where the lateral slope in topography is greatest near the pool. (b) A shear stress contour map illustrates the regions of highest shear stress. Warm colors represent higher shear than cool colors.

4. Discussion

4.1 Selective transport and sorting in gravel vs. sand-bed meanders

The ratio of cross-stream (q_n) to downstream (q_s) unit sediment transport, averaged across each cross section, for fine (< 2 mm) and coarse (> 4 mm) particles is presented in Figure 11. At cross section 10 (8.5 m downstream), the sediment particles finer than 2 mm shift from an outward trajectory (toward the pool) to inward (toward the bar) (see also Figure 12). In this region downstream of the apex at the inside bank, shear stress decreases from 23 to 2 Pa, and the transport becomes size-selective with mostly fine particles moving.

The percentage of total unit transport represented by fine particles (< 2 mm) increases over the bar top, from 3% at cross section 10 to 11% at cross section 11 and then 24% at cross section 12, while the percentage of total transport of coarse particles (> 4 mm) decreases from 15% at cross section 9 down to 6% by cross section 13 and drops below 3% in cross sections 14 and 15. Dietrich & Whiting (1989) observed a similar occurrence of selective fine sediment transport on the bar although the data collected at Rio Grande del Ranchos River were sparse. They suggested that if available, sand may be thrown into suspension in the zone of maximum shear stress at the upstream part of the bend and settle down to travel as bed load over the bar top. We observed transport of fine particles (including sand size) as bed load through the entire bend. Their observations and ours suggest that the divergence of shear stress on the bar top is accommodated by selective transport and deposition of fine material.

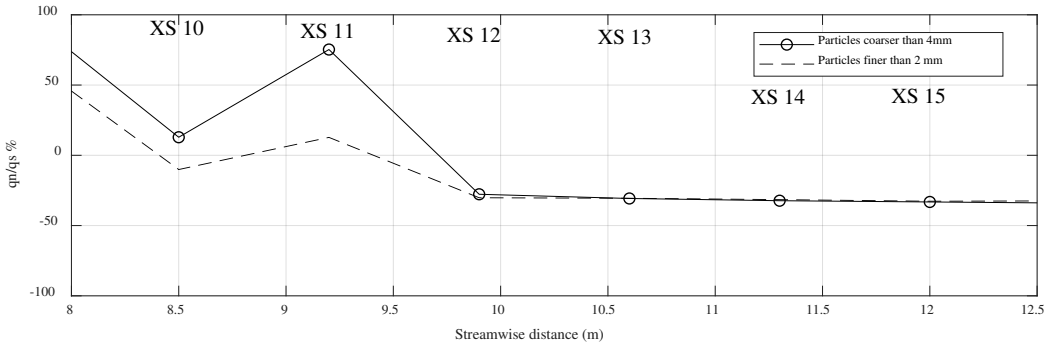

Figure 11. Ratio of transverse to streamwise unit sediment flux for particles coarser than 4 mm and finer than 2 mm. Note that the fine particles have a slight overall negative (toward the right bank) direction as they move toward the bar top. The coarse particles dip to an almost zero value of transverse transport downstream of the bend apex, but remain positive (toward the left bank) as they shift toward the pool.

At cross section 11, the shoaling nature of flow over the bar transports low volumes of available fine sediment particles toward the pool and the q_n/q_s ratio for fine sediment locally returns to a positive value. At cross section 12 and downstream, coarse and fine sediment follow a similar trajectory along the zone of maximum shear stress as they are transported toward the subsequent downstream pool-bar formation.

Although there are slight local differences in the transport trajectories of different sized particles, the loci of maximum transport of large (>4 mm) and fine (<2 mm) particles are nearly identical (Figure 13a). In their studies of sediment transport through a sand-bedded meander bend, Dietrich & Whiting (1989) noticed a drastic difference in the trajectory for a range of particle sizes (Figure 13b). The finest and coarsest class of particles measured moved through the bend out of phase, crossing paths a short distance downstream of the bend apex. This marked difference likely indicates that, although present, varied cross-stream transport by size fraction in gravel is not as significant when producing equilibrium bed topography or roughness patches as it is in sand bedded channels. This is affirmed by observations of helical flows and analysis of Shields stresses. It should be noted that compared to our flume, the sand-bed study had a smaller

radius of curvature and a greater maximum angle of departure influencing the strength of helical flows and possibly sediment trajectories.

(a)

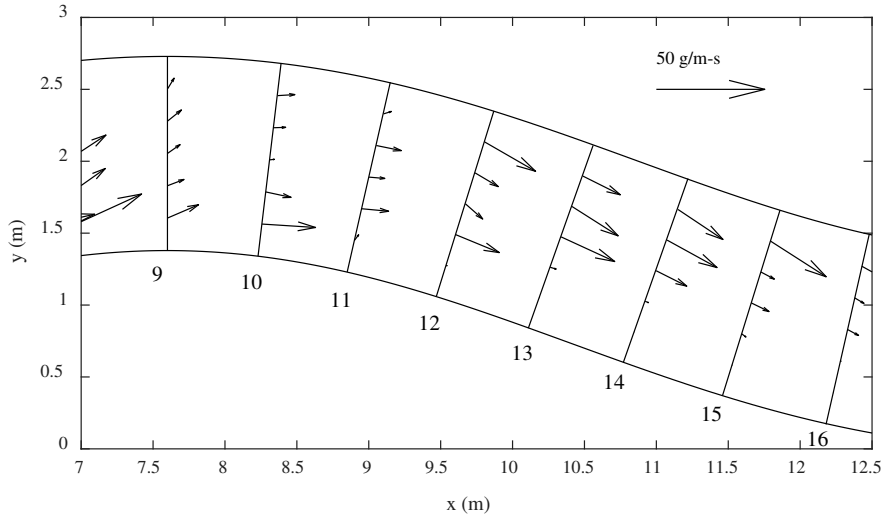

(b)

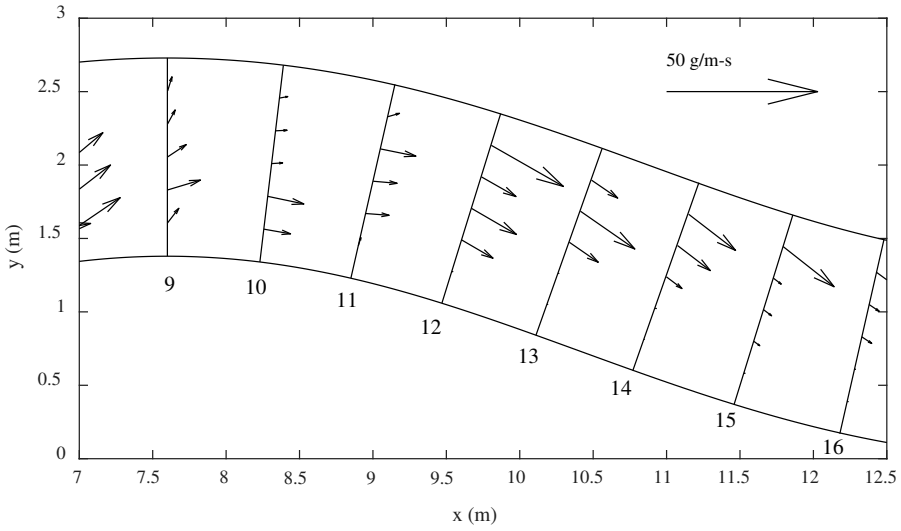

Figure 12 (a) Expanded view of direction and magnitude of unit sediment discharge of particles coarser than 4 mm. (b) Vectors showing direction and magnitude of unit sediment discharge of particles finer than 2 mm in the zone of clearly defined sorting patches.

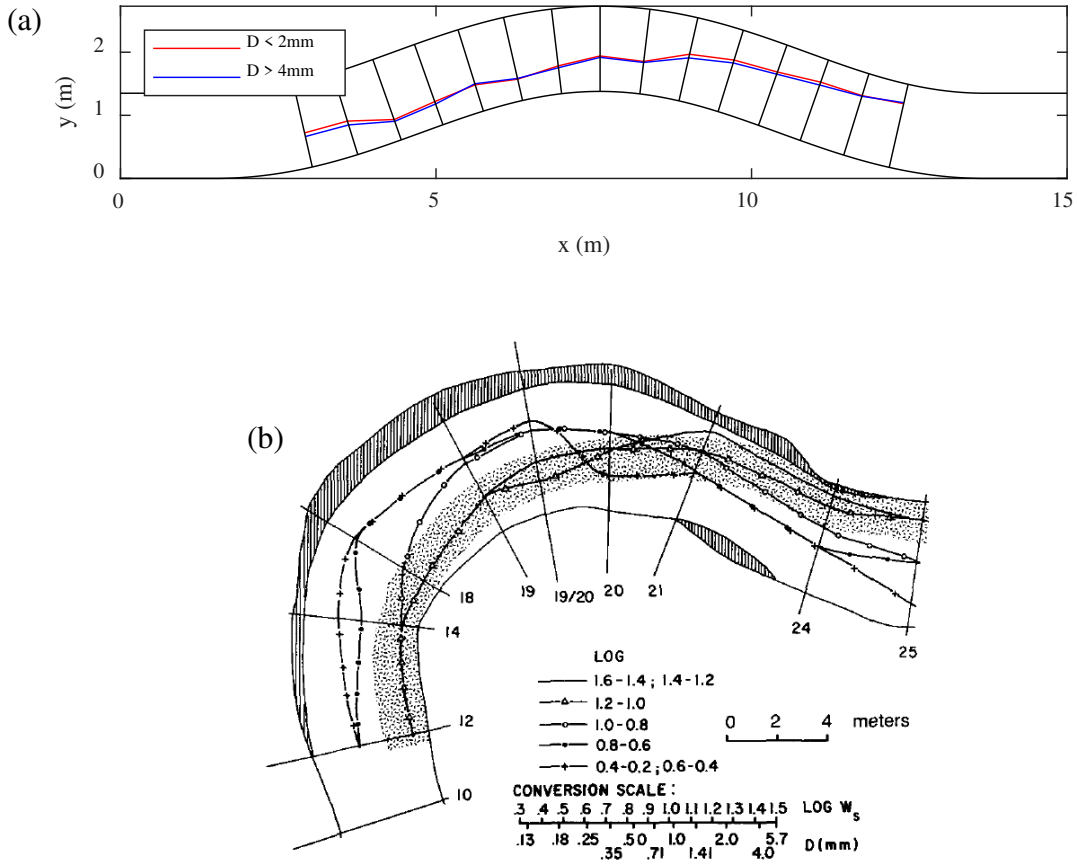

Figure 13 (a)**.** Locus of maximum transport of particles finer than 2 mm (red) and coarser than 4 mm (blue). (b) Dietrich & Whiting (1989) show that in sand bed meander bends, the loci (center of mass) do not follow one another as closely with the fine particles shifting toward the bar at the bend apex. The smallest particles do not follow the region of highest shear (stippled region).

To investigate the possibility that the sorting patterns we observed were at least partially the result of partial or selective transport, we used the shear stress field calculated from our velocity observations to estimate where particles of different size should be mobile, by calculating the dimensionless shear stress (τ^*) and comparing that to a critical value (τ^*_c, taken here to be 0.0386; Parker, 1990). Figure 14 shows regions where the dimensionless stress for 2 mm, 4 mm, and 8 mm sediment exceeds or falls below the critical value, expressed as the stress ratio τ^*/τ^*_c. The stress ratio is well below 1 for 4 mm sediment particles where the finest patch was located,

at the inside of the channel, just downstream of the bend apex. For 2 mm diameter particles, the stress ratio remains well above 1 throughout nearly the entire channel. This indicates that the coarse sediment particles were not fully mobile at all points in the channel, but the fine particles were. The stress ratio for 8 mm particles was less than 1 in the upstream half of the pool but was generally greater than 1 for all smaller particles. Sediment particles larger than 8 mm in diameter made up less than 2% by weight of the sediment mixture fed into the flume. In the region of developed flow (downstream of the apex) they were only found in significant numbers in the deepest part of the pool. This suggests that these large particles armored the pool with fine particles selectively transported inward, upslope to the region of maximum shear stress.

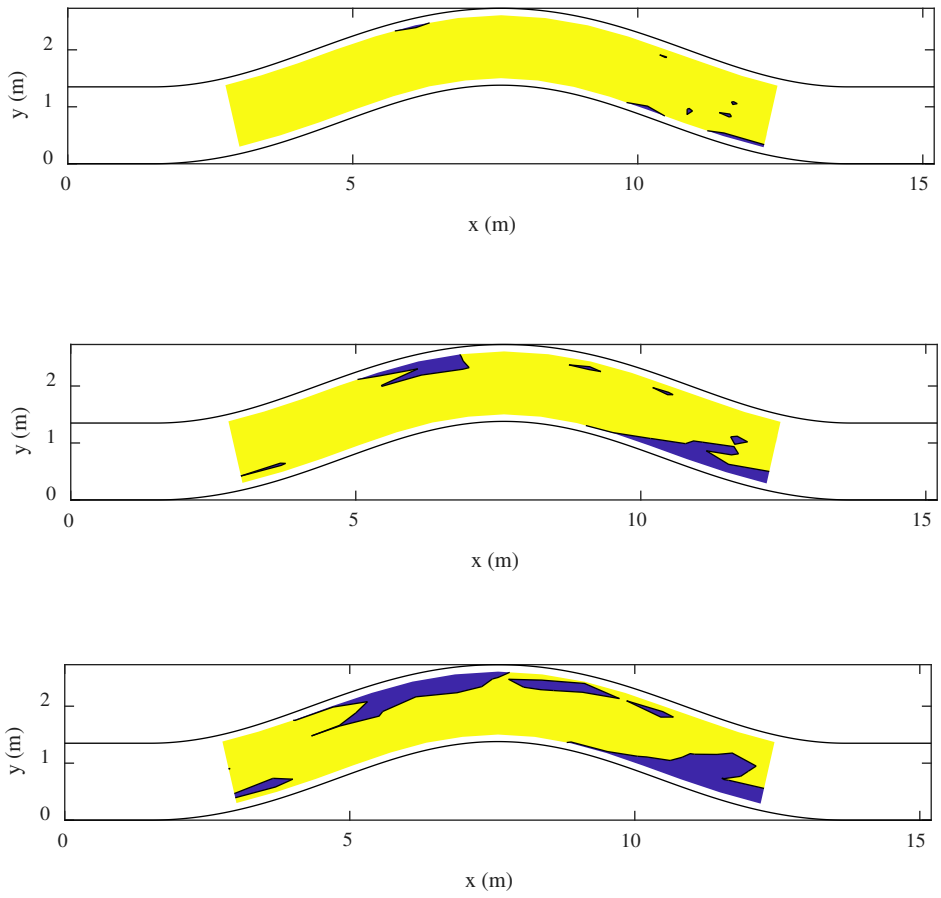

Figure 14. (a) τ^*/τ_c^* for 2 mm sediment is represented where the blue shaded regions represent a ratio less than 1 and the yellow shaded regions, greater than one. At almost all points in the channel, the Shields to reference Shields stress ratio is greater than 1. Particles finer than 2 mm are expected to be mobile throughout the channel. b.) τ^*/τ_c^* for 4 mm sediment; on the bar tops, the ratio exceeds 1 for particles coarser than 4mm, and therefore, particles larger than 4 mm are unlikely to be transported onto the bar. c.) τ^*/τ_c^* for 8 mm sediment; in the upstream half of the pool, the ratio is below zero. This indicates that as coarse particles are transported toward the pool, they will remain there while finer sediment particles are selectively transported through the pool.

4.2 Gravity verses secondary flows

Near the outside edge of the bend calculated shear stress vectors indicate that there is flow convergence along the edge of the pool. This convergent flow corresponds with the transition from the coarsest observed bed load patch (D_{50} = 3.6 mm) to a medium patch (D_{50} = 2.3 mm). The shear stress magnitude in upper half of the pool is not high compared to the other regions in the channel. The shear stress in the pool does not increase with sediment size, indicating that selective transport of fine particles by secondary currents plays an important role in the development of coarsest patches. The largest particles (> 8 mm) were only observed in the pools, probably because the strong gravitational forces on the side slope of the bar were greater than upslope forces from secondary currents. The secondary currents were confined to the deepest part of the upstream half of the pool and effectively shunted smaller particles inward laterally upslope toward the zone of maximum shear stress where the bar transitions to the pool.

In the patch of finest sediment particles ($D_{50} = 1.5\ mm$) past the bend apex, there is a very low lateral slope. The average lateral slope for cross sections 12 and 13 in the fines patch was 0.2% compared to an average slope through the whole cross section of 20%. This leads us to conclude that gravitational forces associated with particles rolling toward the pool have little effect here. A divergence of both shear stress and sediment transport is the controlling factor in the deposition of fine particles on the bar. Near the pool, however, the flat bar top transitions to a steep slope into the pool where both the effects of gravity and secondary currents are present. Coarse particles were found in the pool, having been more strongly affected by gravitational forces than the inward-directed near bed velocity. There is a shortage of investigations into the effects that varied degrees of meandering and other planform geometry have on the extent of secondary currents and their influence on sorting of both sand and gravel beds. A study of this

nature would prove meaningful in identifying thresholds at which certain mechanisms for sorting are strongest.

5. Conclusion

To our knowledge, this study involving coupled observations of bed load transport by size fraction, near-bed velocity, calculated shear stress, and quasi-equilibrium bed topography leading to clearly sorted patches is the first of its kind in a gravel-bed meandering channel. We were able to measure each element at high resolution due to the controlled flume environment. In our experiment, spatial variations in shear stress led to conditions where, locally, coarser fractions of the grain-size distribution could become immobile, and this development of partial and selective transport is primarily responsible for the persistence of coarse pools and fine bars. This contrasts with sand-bedded meandering channels, where generally all particle sizes are fully mobile and sorting is more dependent on the balance of secondary flows and gravitational effects. We show that although the trajectories of coarse and fine particles are varied in localized regions of the meander bend, the maximum transport of all particle sizes occurs in the corridor of greatest shear stress, which was also different from observations in a sand-bedded channel. In pools, secondary currents produce near-bed, upslope shear that counteracts gravitational forces. The effects of this secondary flow were constrained to the deepest part of the pool and coarsest sorted patch until well past the bend apex. Extent of secondary currents and their influence on sorting is a function of planform geometry. These observed mechanisms suggest that divergence in boundary shear stress is accommodated by spatially varied preferential bed load transport, resulting in persistent sorted patches of varying degrees of roughness and equilibrium conditions.

References

Bridge, J. S. (1977). Flow, bed topography, grain size and sedimentary structure in open channel bends: A three-dimensional model. *Earth Surface Processes*, *2*(4), 401–416. https://doi.org/10.1002/esp.3290020410

Buffington, J. M., & Montgomery, D. R. (1999). A Procedure for classifying textural facies in gravel-bed rivers. *Water Resour. Res.*, *35*(6), 1903–1914. https://doi.org/10.1029/1999WR900041

Chapman, D. W. (1988). Critical Review of Variables Used to Define Effects of Fines in Redds of Large Salmonids. *Transactions of the American Fisheries Society*, *117*(1), 1–21. https://doi.org/10.1577/1548-8659(1988)117<0001:CROVUT>2.3.CO;2

Clayton, J. A. (2010). Local sorting, bend curvature, and particle mobility in meandering gravel bed rivers: TECHNICAL NOTE. *Water Resour. Res.*, *46*(2), 371. https://doi.org/10.1029/2008WR007669

Clayton, J. A., & Pitlick, J. (2007). Spatial and temporal variations in bed load transport intensity in a gravel bed river bend. *Water Resour. Res.*, *43*(2), 371. https://doi.org/10.1029/2006WR005253

Clayton, J. A., & Pitlick, J. (2008). Persistence of the surface texture of a gravel-bed river during a large flood. *Earth Surf. Processes Landforms*, *33*(5), 661–673. https://doi.org/10.1002/esp.1567

Dietrich, W. E. (1987). Mechanics of Flow and Sediment Transport in River Bends. In K. S. Richards (Ed.), *River Channels: environment and process* (pp. 129–158). Basil Blackwell.

Dietrich, W. E., & Smith, J. D. (1984). Bed Load Transport in a River Meander. *Water Resources Research*, *20*(10), 1355–1380. https://doi.org/10.1029/wr020i010p01355

Dietrich, W. E., & Whiting, P. (1989). Boundary shear stress and sediment transport in river meanders of sand and gravel. *Water Resources Monograph*, 1–50. https://doi.org/10.1029/wm012p0001

Ikeda, S. (1989). Sediment Transport and Sorting at Bends. In *River Meandering* (pp. 103–125). American Geophysical Union (AGU). https://doi.org/10.1029/WM012p0103

Jackson, R. G. (1975). Velocity–bed-form–texture patterns of meander bends in the lower Wabash River of Illinois and Indiana. *GSA Bulletin*, *86*(11), 1511–1522. https://doi.org/10.1130/0016-7606(1975)86<1511:VPOMBI>2.0.CO;2

Julien, P. Y., & Anthony, D. J. (2002). Bed load motion and grain sorting in a meandering stream. *J. Hydraul. Res.*, *40*(2), 125–133. https://doi.org/10.1080/00221680209499855

Keller, E. A., & Florsheim, J. L. (1993). Velocity-reversal hypothesis: A model approach. *Earth Surf. Processes Landforms*, *18*(8), 733–740. https://doi.org/10.1002/esp.3290180807

Kondolf, G. M., & Wolman, M. G. (1993). The sizes of salmonid spawning gravels. *Water Resources Research*, *29*(7), 2275–2285. https://doi.org/10.1029/93WR00402

Langbein, W. B., & Leopold, L. B. (1966). *River meanders - Theory of minimum variance* (Professional Paper). https://doi.org/10.3133/pp422H

Lanzoni, S. (2000). Experiments on bar formation in a straight flume: 2. Graded sediment. *Water Resources Research*, *36*(11), 3351–3363. https://doi.org/10.1029/2000WR900161

Leopold, L. B., & Wolman, M. G. (1957). *River channel patterns: Braided, meandering, and straight* (USGS Numbered Series No. 282- B) (p. 50). Washington, D.C.: U.S. Government Printing Office. Retrieved from http://pubs.er.usgs.gov/publication/pp282B

Lisle, T. E., & Madej, M. A. (1992). Spatial variation in armouring in a channel with high sediment supply, 17.

Nelson, P. A., Venditti, J. G., Dietrich, W. E., Kirchner, J. W., Ikeda, H., Iseya, F., & Sklar, L. S. (2009). Response of bed surface patchiness to reductions in sediment supply. *Journal of Geophysical Research: Earth Surface*, *114*(F2). https://doi.org/10.1029/2008JF001144

Nelson, P. A., Dietrich, W. E., & Venditti, J. G. (2010). Bed topography and the development of forced bed surface patches. *J. Geophys. Res.*, *115*(F4), 199. https://doi.org/10.1029/2010JF001747

Paola, C., & Seal, R. (1995). Grain Size Patchiness as a Cause of Selective Deposition and Downstream Fining. *Water Resources Research*, *31*(5), 1395–1407. https://doi.org/10.1029/94WR02975

Parker, G. (1990). Surface-based bedload transport relation for gravel rivers. *Journal of Hydraulic Research*, *28*(4), 417–436. https://doi.org/10.1080/00221689009499058

Parker, Gary, & Andrews, E. D. (1985). Sorting of Bed Load Sediment by Flow in Meander Bends. *Water Resources Research*, *21*(9), 1361–1373. https://doi.org/10.1029/wr021i009p01361

Powell, D. M. (1998). Patterns and processes of sediment sorting in gravel-bed rivers. *Progress in Physical Geography: Earth and Environment*, *22*(1), 1–32. https://doi.org/10.1177/030913339802200101

Smith, J. D., & Mclean, S. R. (1984). A Model for Flow in Meandering Streams. *Water Resources Research*, *20*(9), 1301–1315. https://doi.org/10.1029/WR020i009p01301

Thompson, D. M., Wohl, E. E., & Jarrett, R. D. (1999). Velocity reversals and sediment sorting in pools and riffles controlled by channel constrictions. *Geomorphology*, *27*(3–4), 229–241. https://doi.org/10.1016/s0169-555x(98)00082-8

van Rijn Leo C. (2007). Unified View of Sediment Transport by Currents and Waves. I: Initiation of Motion, Bed Roughness, and Bed-Load Transport. *Journal of Hydraulic Engineering*, *133*(6), 649–667. https://doi.org/10.1061/(ASCE)0733-9429(2007)133:6(649)

Venditti, J. G., Dietrich, W. E., Nelson, P. A., Wydzga, M. A., Fadde, J., & Sklar, L. (2010). Mobilization of coarse surface layers in gravel-bedded rivers by finer gravel bed load. *Water Resources Research*, *46*(7). https://doi.org/10.1029/2009WR008329

Wilcock, P. R. (1996). Estimating Local Bed Shear Stress from Velocity Observations. *Water Resources Research*, *32*(11), 3361–3366. https://doi.org/10.1029/96WR02277

Wilcock, P. R., & Crowe, J. C. (2003). Surface-based Transport Model for Mixed-Size Sediment. *Journal of Hydraulic Engineering*, *129*(2), 120–128. https://doi.org/10.1061/(ASCE)0733-9429(2003)129:2(120)

Wood, P. J., & Armitage, P. D. (1997). Biological Effects of Fine Sediment in the Lotic Environment. *Environmental Management*, *21*(2), 203–217. https://doi.org/10.1007/s002679900019

Appendix A. Experiment setup photos

Figure A1. We used a Helley-Smith bed load sampler and sampled over periods ranging from 45 to 120 seconds. The bottom picture shows our velocity measurement configuration using a Vectrino ADV which we mounted to a rolling track.

Figure A2. These two pictures show the flume set up with water being pumped and sediment fed into the channel. The picture on the left is looking upstream and the figure on the right is looking downstream.

Appendix B. NaysCUBE 3D hydrodynamic model results

We used the equilibrium bed topography to define the grid shape and geographic data and ran a 3D hydrodynamic simulation using the NaysCUBE solver, included the iRIC suite of hydrodynamic and morphodynamic models (www.i-ric.org). Here were compare the model-simulated shear stress values with those calculated using the velocity profile log law calculations. The calculation conditions used in the 3D model are as follows: we used a non-liner $\kappa - \epsilon$ turbulence model with a fixed bed to simulate the equilibrium bed conditions at constant discharge. The downstream boundary condition was a measured constant WSEL of 9.97 m above the local datum throughout the experiment. We set spatially varied bed roughness values based on the observed sediment sorting patches using the following relation: $n \cong 0.062 D_{50}^{1/6}$.

A statistical regression of the modeled and measured water surface elevations returns an R^2 of 0.65 and a Root Mean Squared Error (RMSE) of 2 centimeters (see Figure B1). Adjustment of the roughness values, and other modifications to the model could have resulted in a more closely approximated water surface elevation, however, we did not feel that such adjustment was warranted as our goal in running a hydraulic model was simply to compare shear stress magnitude and pattern with those measured in the flume.

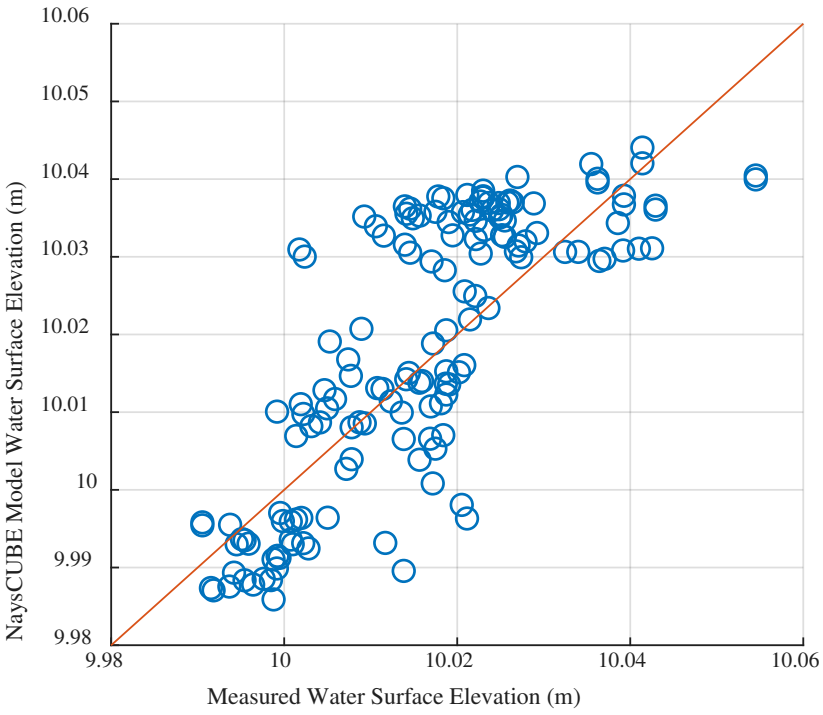

Figure B1. Regression of NaysCUBE modeled water surface elevations vs. measured values in the flume.

The modeled shear stress patterns bear a similar resemblance to measured shear stress. The region of highest shear stress was located near the bend apex and it transitions to the left side of the channel at the tail of the pool. The modeled shear stress patterns are spatially correlated with the regions of high sediment transport. The modeled shear stress patterns affirm the observation that shear stress does not spatially correlate uniformly with sediment particle size on the bed.

The magnitude of modeled shear stresses is significantly less than those calculated using the log-law velocity profile relations. The shear stress calculation performed in the model uses an estimated velocity value near the bed defined as half the height of the computational cell closest to the bed. The model domain was discretized into 10 vertical nodes and as such, the value used

in calculation of u_* at each grid may not be high enough resolution to correctly represent near bed velocity patterns. Equation B1 is used in NaysCUBE to calculate the shear velocity.

$$\frac{u(z)}{u_*} = \frac{1}{\kappa}\ln\left(\frac{\Delta\zeta/2}{k_s}\right) + A_s \tag{B1}$$

where $\kappa = 0.4$, u is the computed velocity at a height $\Delta\zeta/2$ above the bed, where $\Delta\zeta$ is the height of the computational cell near the bed, k_s is the roughness height evaulated as $k_s = 0.4D_{50}$ when the grain size is given or when using Manning's equation to define roughness, equation B2 is used. Because spatially varied bed grain size is not incorporated into the model, the roughness height was calculated from our estimate of Manning's n as previously described.

$$n = \frac{k_s^{1/6}}{7.66\sqrt{g}} \tag{B2}$$

In order to more accurately model the velocities that are happening at high resolution scales, the computational grid must be much finer. Running a 3D hydrodanmic model with such fine resolution is computationally expensive and time intensive. For the purposes of this study, a comparison of the model output at this scale is sufficient. We will likely perform further analysis of the model output at finer resolution in continued study of the results of this experiment.

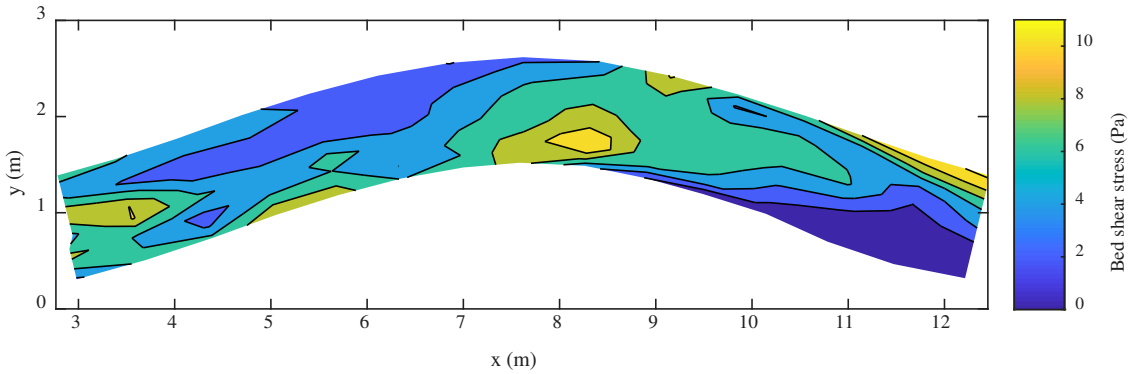

Figure B2. Bed shear stress as modeled in NaysCUBE. The pattern matches the calculated bed shear stress from velocity measurements, however, the values calculated from the velocity profile measurements are much higher than the numerical solution.

Appendix C Velocity profiles at 15 measured cross sections

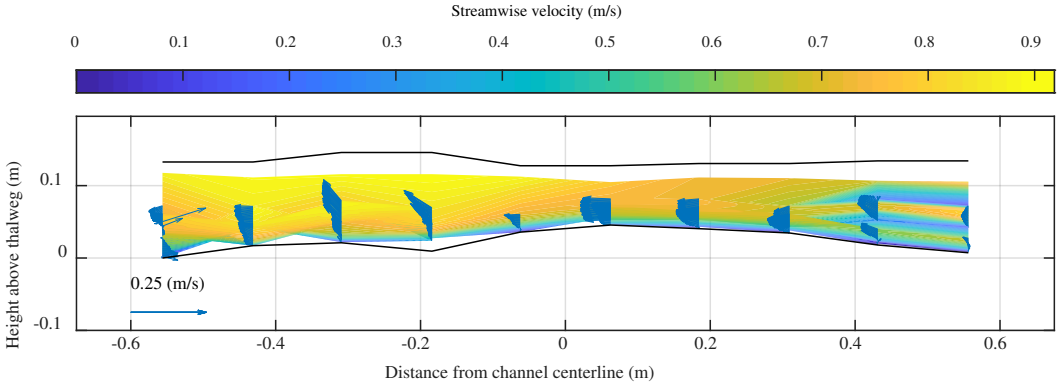

Figure D1. Velocity profile at the upstream-most cross section (2)

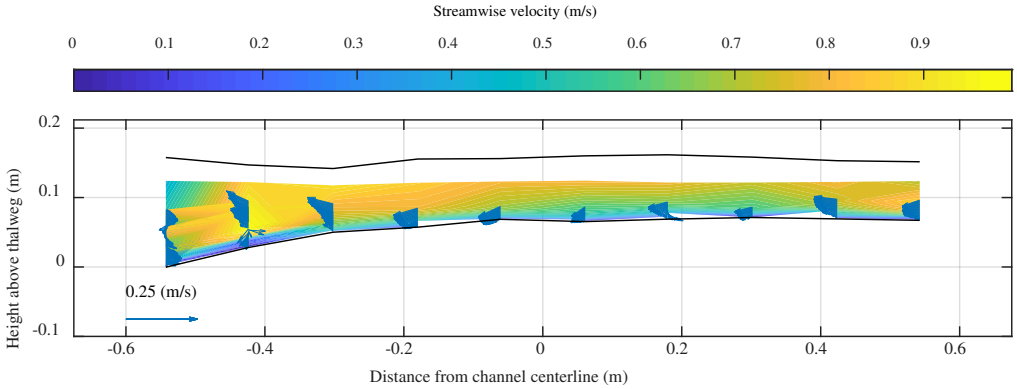

Figure D2. Velocity profiles at cross section 3

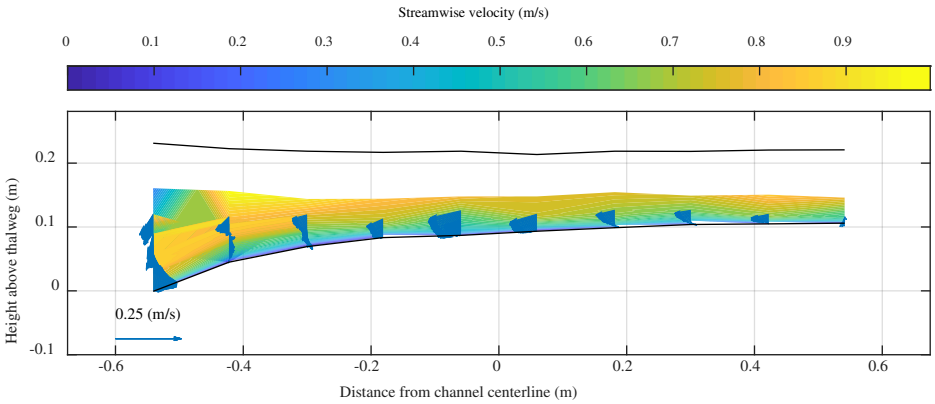

Figure D3. Velocity profiles at cross section 4

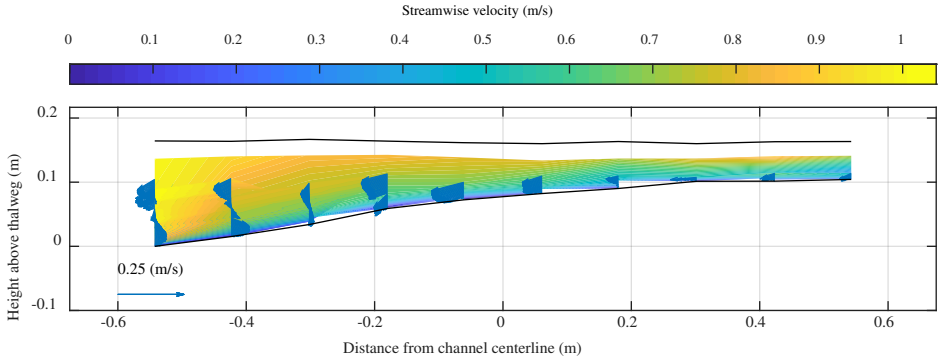

Figure D4. Velocity profiles at cross section 5

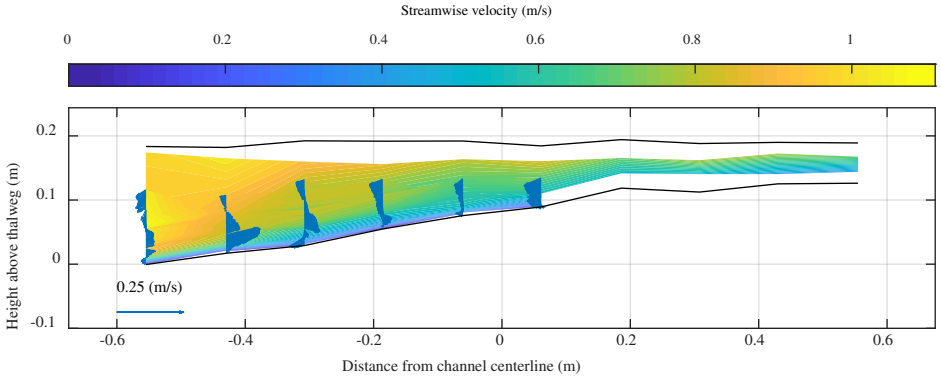

Figure D5. Velocity profies at cross section 6

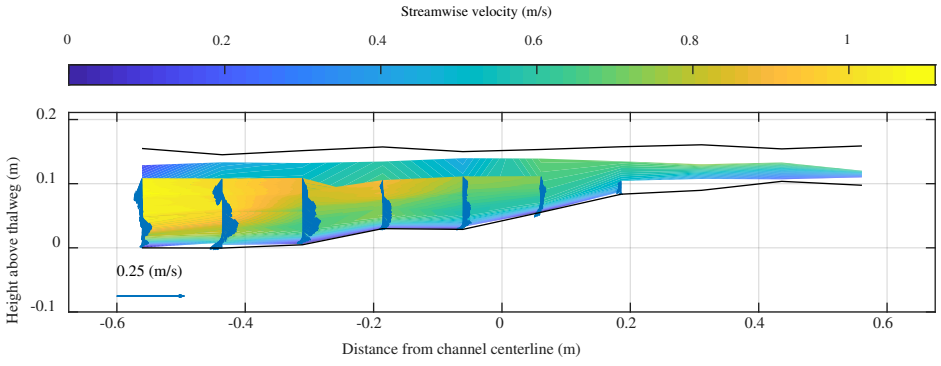

Figure D6. Velocity profiles at cross section 7

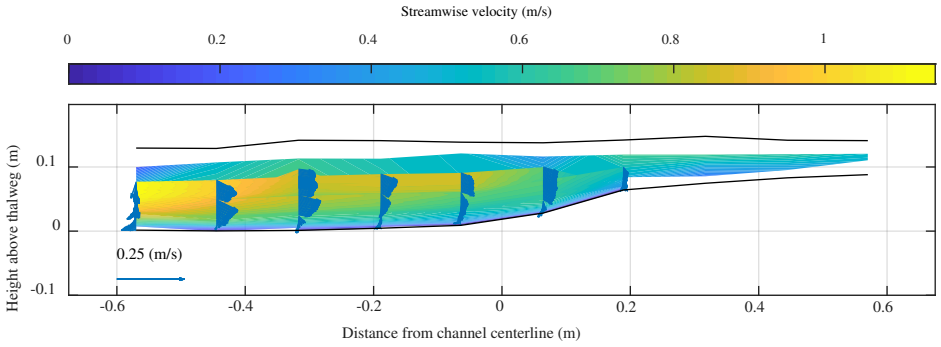

Figure D7. Velocity profiles at cross section 8

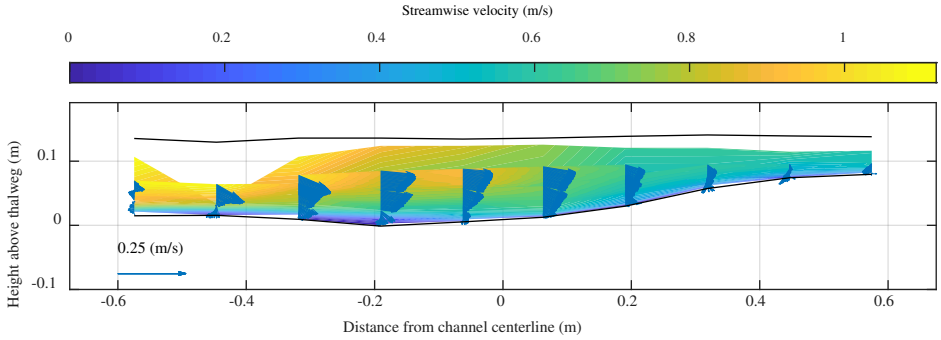

Figure D8. Velocity profiles at cross section 9, at the bend apex.

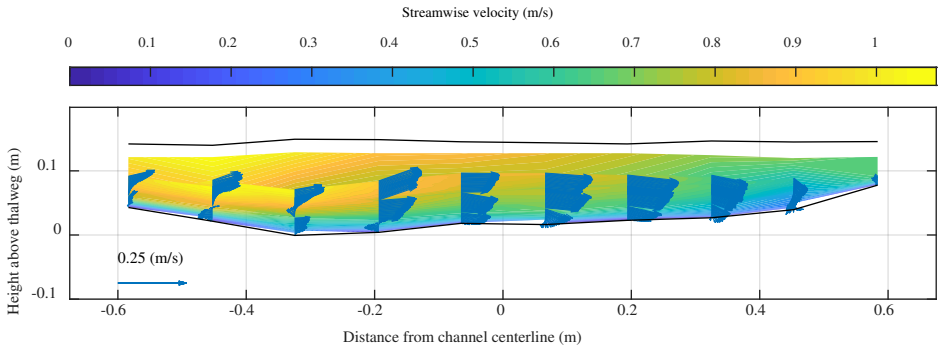

Figure D9. Velocity proifles at cross section 10.

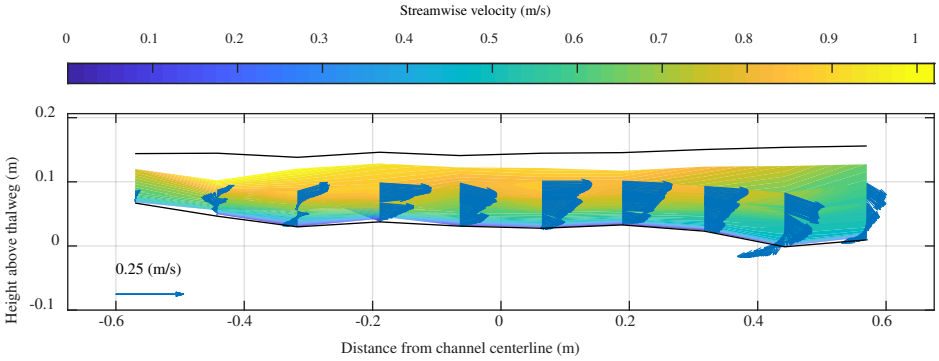

Figure D10. Velocity profiles at cross section 11.

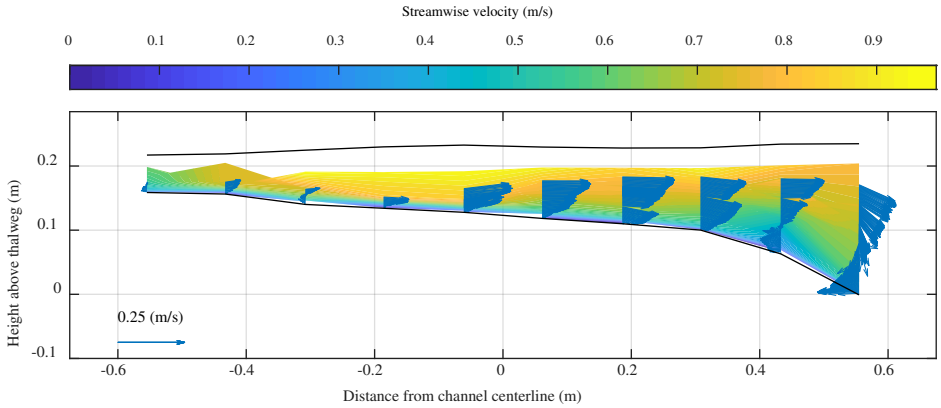

Figure D11. Velocity profiles at cross section 12.

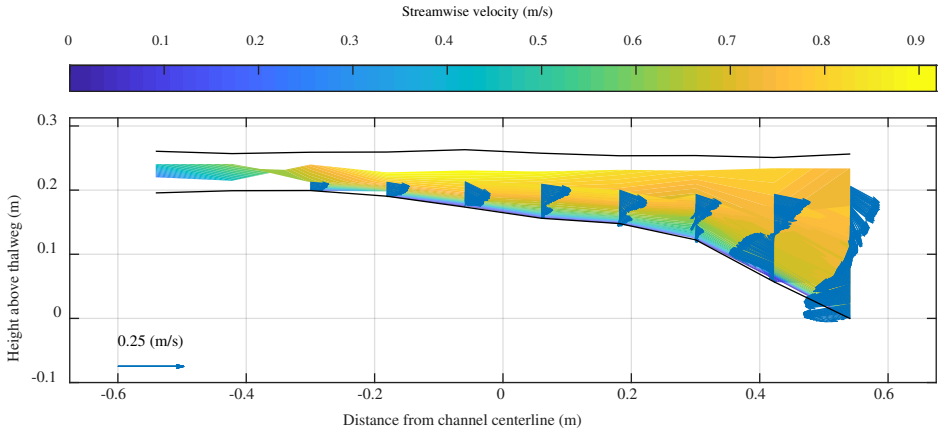

Figure D12. Velocity profiles at cross section 13.

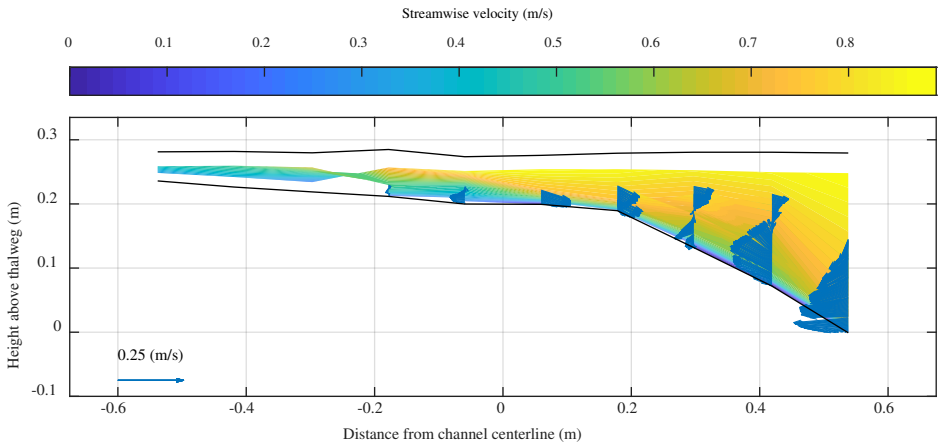

Figure D13. Velocity profiles at cross section 14.

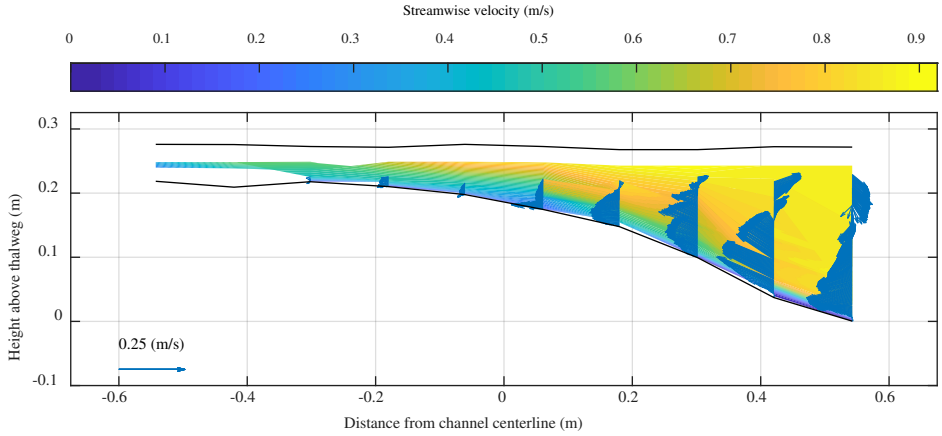

Figure D14. Velocity profiles at cross section 15.

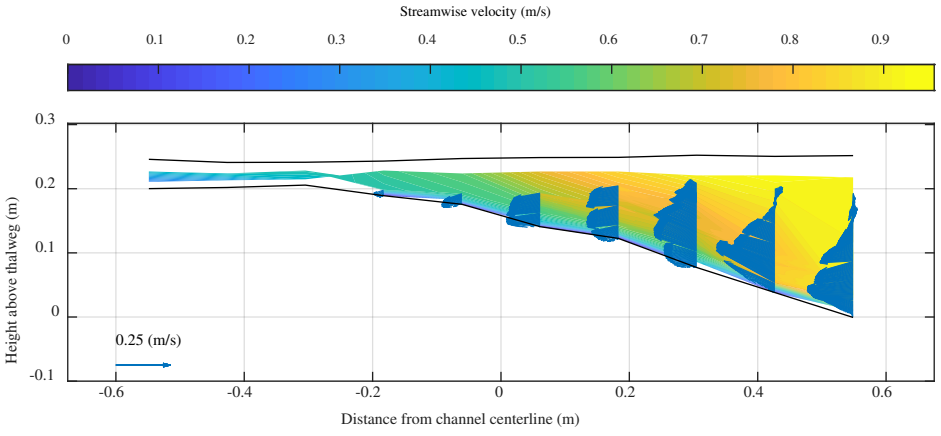

Figure D15. Velocity profiles at cross section 16.

Appendix D. Equilibrium bed sediment sorting

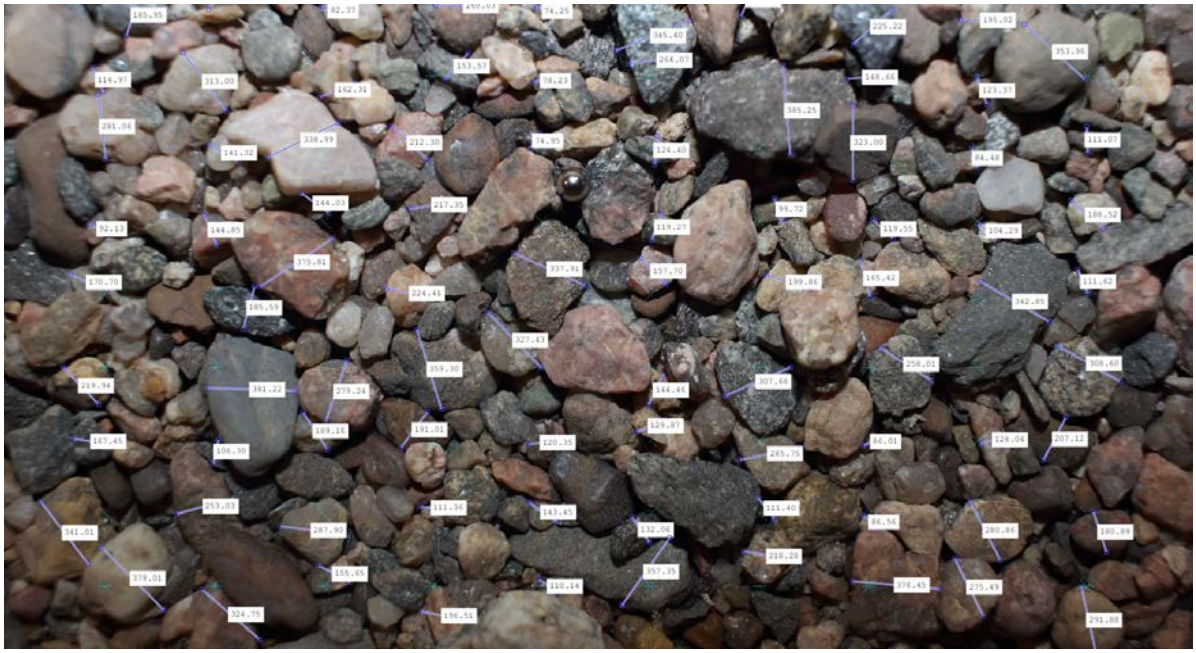

Figure E1. Grid by number pebble count image. 100 Evenly spaced points were place on the photo. At the location of each of the points, we measured the pixel length of the intermediate axis of the particle located directly under the point. If particles were deeply imbricated, we systematically chose the closest particle up and to the left and measured its intermediate axis. A small ball bearing was placed in the photos at the same height as the particles and measured in pixels to assign a pixel per mm value for each photo analyzed for pebble counts.

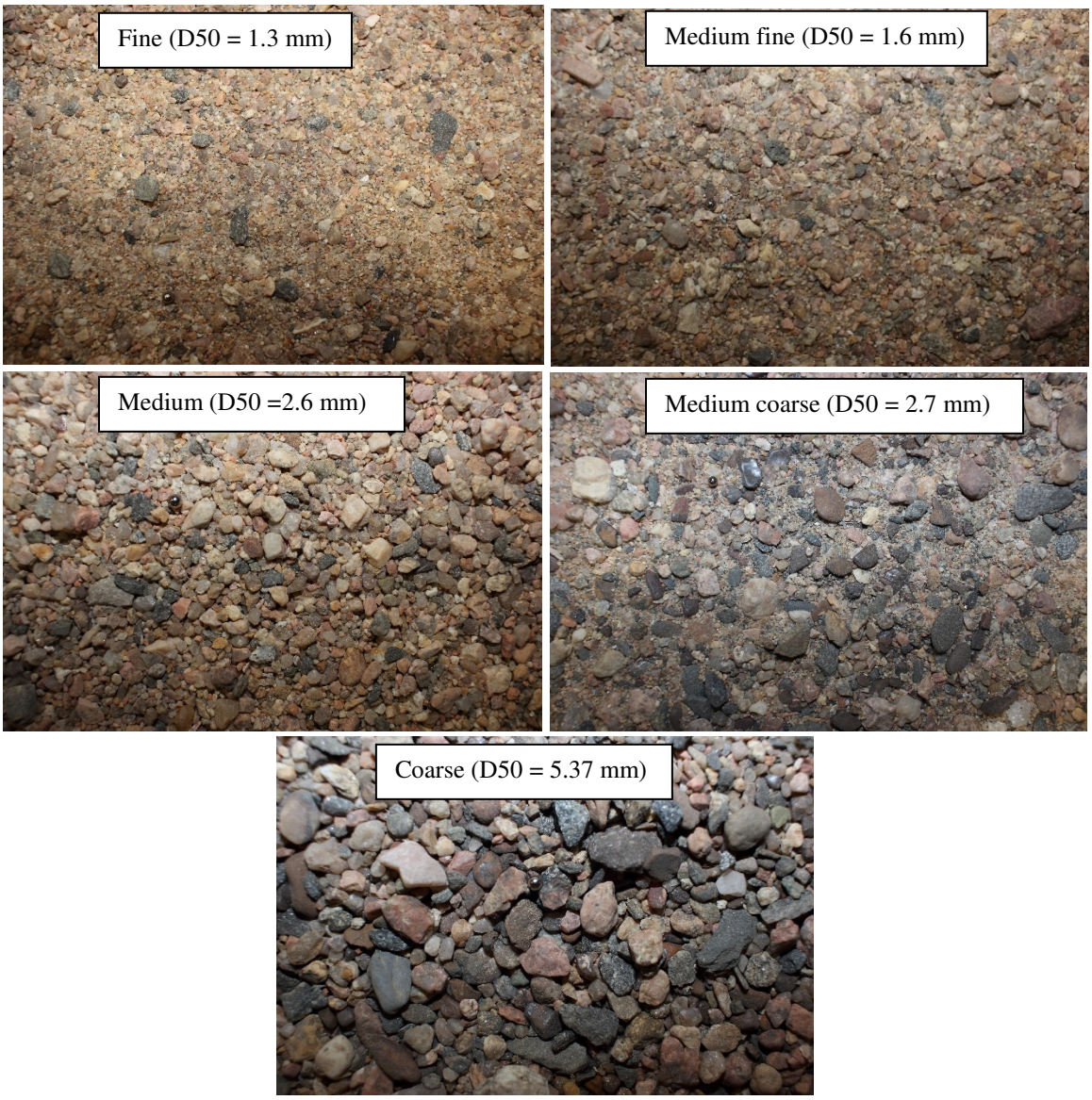

Figure E2. Scaled photos taken of each of the visually delineated sorting patches throughout the channel.